
Article:
Sun, G., Mitchell, R.L., Chen, Z. et al. (5 more authors) (2025) 3D tensile fracture analysis of tailored fibre placement composites using digital volume correlation. Theoretical and Applied Fracture Mechanics, 140. 105127. ISSN: 0167-8442

https://doi.org/10.1016/j.tafmec.2025.105127

3D Tensile Fracture Analysis of Tailored Fibre Placement Composites using Digital Volume Correlation

Guowen Sun[a], Ria L Mitchell[b], Zilei Chen[a], Fatma Omrani[c], Matt Smith[c], Clara Frias[c], J. Patrick A. Fairclough[a], Christophe Pinna[a*]

[a] The School of Mechanical, Aerospace and Civil Engineering, The University of Sheffield, Sheffield, S1 3JD, United Kingdom

[b] Sheffield Tomography Centre, The University of Sheffield, Sheffield, S1 3JD, United Kingdom, now at ZEISS Microscopy

[c] Advanced Manufacturing Research Centre, The University of Sheffield, Sheffield, S60 5TZ, United Kingdom

[*]Corresponding author: c.pinna@sheffield.ac.uk.

Abstract

Tailored Fibre Placement (TFP) composites, manufactured using one of the latest dry-fibre technologies, feature unique 3D fibre bundle architectures and complex layup configurations involving stitching threads and base materials. Damage development under load is therefore challenging to observe and failure hard to predict. In this study, in-situ tensile testing of a TFP composite was conducted for the first time within an X-ray Computed Tomography microscope to capture the 3D damage evolution up to failure. Segmented image-based models were used to correlate crack locations with strain distributions measured using Digital Volume Correlation by post-processing X-ray images recorded at regular load intervals throughout the test. Results revealed that initial

cracks appeared at applied stresses below 50% UTS, and propagated mainly within fibre bundles. The first initiation site matched the location of the maximum value (about 0.008) of the local strain component transverse to the fibre direction within the ply where the first crack appeared. Propagation followed bands of strain concentration along the fibre bundle direction, first in off-axis plies and then in longitudinal plies towards the end of the test, with the crack volume fraction increasing exponentially after initiation. Very limited delamination was observed after 90% UTS, with stitching threads thought to be responsible for this retardation. Results therefore showed that fracture can be controlled through optimisation of the manufacturing process and laminate design. They also provide the foundation for the future development of physically-based multiscale strength prediction models needed for this optimal design of TFP composites for lightweight structural applications.

Keywords: Tailored Fibre Placement; Digital Volume Correlation; Damage initiation; 3D fracture characterisation; In-situ tensile testing.

1 Introduction

Tailored Fibre Placement (TFP) composites have emerged as a promising class of advanced fibre reinforced materials, offering superior mechanical performance and unprecedented design flexibility [1]. By precisely controlling fibre trajectories, the TFP technology can tailor the mechanical response of composites and optimise their load-bearing capacity [2]. Consequently, these materials have attracted significant interest

across aerospace [3], automotive [4], and sport equipment industries [5], where lightweight and high-performance structural integrity is critical.

However, the durability and structural reliability of TFP composites can be undermined by the lack of understanding of damage development in their complex architecture, which includes fibre bundles laid along predefined paths and secured by stitching threads onto base materials [6]. The introduction of stitching threads and associated manufacturing parameters (e.g., stitch length, stitch width, thread tension) results in pronounced local heterogeneities, leading to highly non-uniform strain fields. These microstructural complexities make the prediction of damage evolution and overall mechanical behaviour challenging. Numerical investigations on TFP composites to date have primarily focused on stiffness prediction and local stress-strain distributions [7]. Strength prediction models remain inexistant so far in the literature, mainly due to the lack of experimental evidence about 3D damage development under load in TFP composites needed for the development and validation of these models. The challenges associated with the observation and analysis of damage evolution in the complex three-dimensional internal structure of these composites are therefore the focus of this study with the aim of filling this experimental gap.

Experimentally, techniques such as Scanning Electron Microscopy (SEM) and two-dimensional Digital Image Correlation (DIC) have been used to study crack initiation in composite materials [8, 9]. While SEM provides detailed fractographic analysis and DIC effectively maps surface strain fields, these techniques are inherently limited in capturing

the complex three-dimensional internal deformation mechanisms crucial to understand damage initiation in TFP composites. Digital Volume Correlation (DVC), a three-dimensional extension of DIC coupled with X-ray Computed Tomography (XCT) and in-situ mechanical loading, has emerged as a powerful alternative, providing comprehensive three-dimensional measurements of internal strain fields [10].

While recent studies have successfully applied DVC in combination with XCT to characterise the internal deformation of composite materials, these efforts have primarily focused on composites with relatively simple and regular fibre architectures. For example, Lee at al. [11] utilised DVC to investigate the subsurface strain distributions in unidirectional laminated composites, focusing primarily on deformation analysis without directly addressing damage initiation or crack morphology. Holmes et al. [12] further explored woven glass fibre composites, demonstrating the capability of DVC to capture out-of-plane strain fields, although their analysis did not include detailed segmentation or quantitative characterisation of cracks. Investigations into damage processes in highly heterogeneous and architecturally complex composites with 3D strain measurements to analyse crack development are therefore lacking in the literature. This study will therefore also focus on addressing this experimental gap.

This study investigates 3D damage development up to fracture in TFP composites by carrying out in-situ tensile testing with XCT. Recorded images at regular intervals during the test are subsequently processed using a systematic local-global DVC procedure to compute volumetric strain distributions and their evolution throughout the test. Local

deformation, crack initiation and propagation are then analysed in relation to local strain distributions. To the authors' knowledge, this is the first comprehensive study of the 3D deformation and damage evolution in TFP composites under tensile loading. By addressing this scientific gap, the results of this work provide a foundation for developing physically-based multiscale models aimed at accurately predicting the strength and damage tolerance of TFP composites. Such models are necessary to maximise the structural integrity of these composites for critical lightweight applications, such as in the aerospace and automotive industries, and for the optimisation of the TFP process.

2 Methods

2.1 Materials and specimen preparation

The TFP composite investigated in this study comprises carbon fibres as the primary reinforcement, stitched onto a base material made of a glass fibre satin weave fabric. The reinforcement consists of 12K carbon fibre tows supplied by Toray Industries (Japan), secured onto the base material using a Serafil Comphil 180 polyester stitching thread. Stitching parameters were set at a stitch length of 7 mm and a stitch width of 5 mm, for the manufacturing of a composite preform with a symmetric $[0/60/-60]_s$ layup sequence. The composite laminates were then infused and cured with a LY 564 epoxy resin mixed with Aradur 2954 hardener. The curing process involved initial heating at 80°C for 1 hour, followed by a post-curing process at 140 °C for 8 hours, specifically chosen to ensure thorough polymerisation and to reduce residual stresses. The resulting TFP composite

panels exhibited a nominal carbon fibre volume fraction of approximately 50% and a thickness of 3.6 mm.

After curing, a dog-bone shaped specimen was cut from a composite panel using a waterjet cutting process to minimise potential thermal and mechanical damage. The specimen geometry (shown in Figure 1 (a)) was specifically designed to be compatible with the maximum load capacity of the in-situ tensile stage while minimising the gauge length to capture all damage events within the Field of View (FOV) during X-ray scanning. Figure 1 (b) shows an XCT cross-section of the gauge length of the specimen where the actual structure of the TFP composite, including the 6 layers of fibre bundles and vertical stitching threads, can be seen after manufacture.

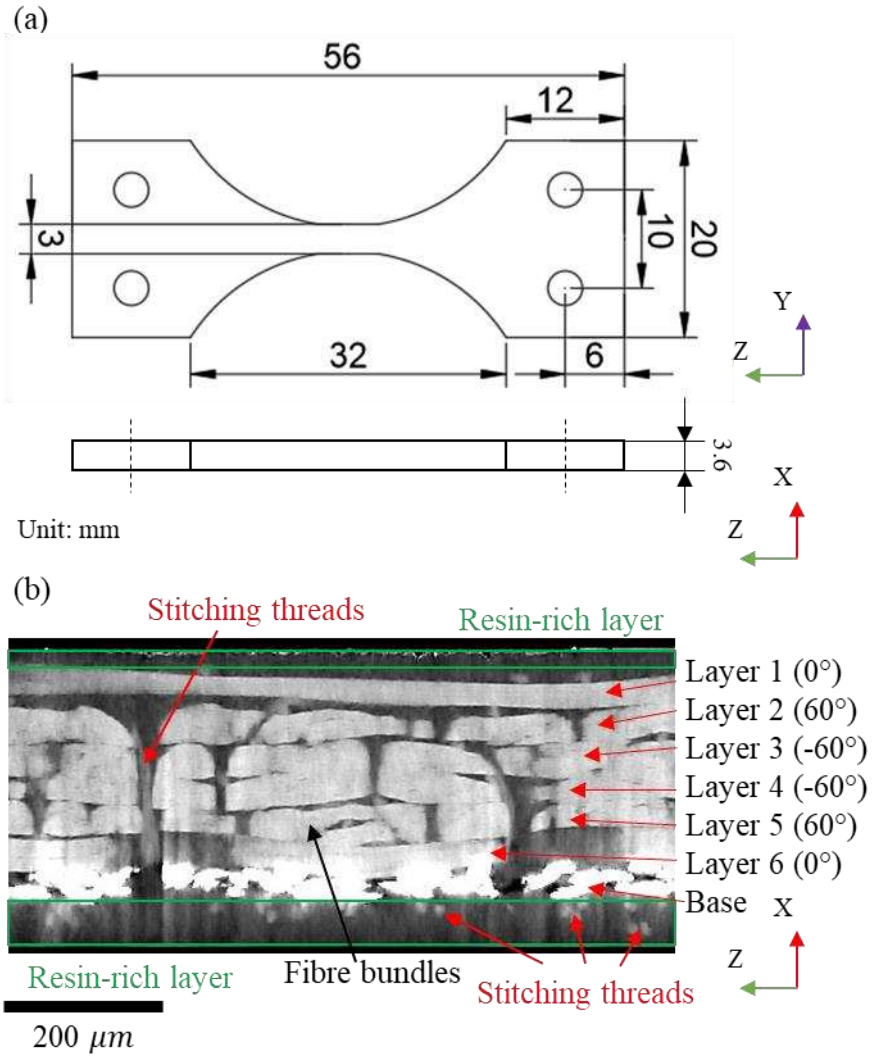

Figure 1: (a) Geometry of the in-situ tensile specimen, showing all key dimensions in millimetres, and (b) 2D XCT image of the TFP specimen showing the XZ view of a through-thickness cross-section. Key microstructural features are identified, including fibre bundles, stitching threads, resin-rich layers, and the stitched fibre architecture across six layers

2.2 Experimental setup and procedures

The experimental setup for concurrent in-situ tensile loading and three-dimensional X-ray tomography imaging is illustrated in Figure 2. A Zeiss Versa 620 X-ray Microscope

(XRM), equipped with a 5kN Deben CT5000TEC tensile stage, was used for in-situ testing. The TFP composite specimen was securely attached to the jaws via four steel pins inserted through dowel holes to ensure stable load transfer and minimal specimen movement (Figure 2 (a)).

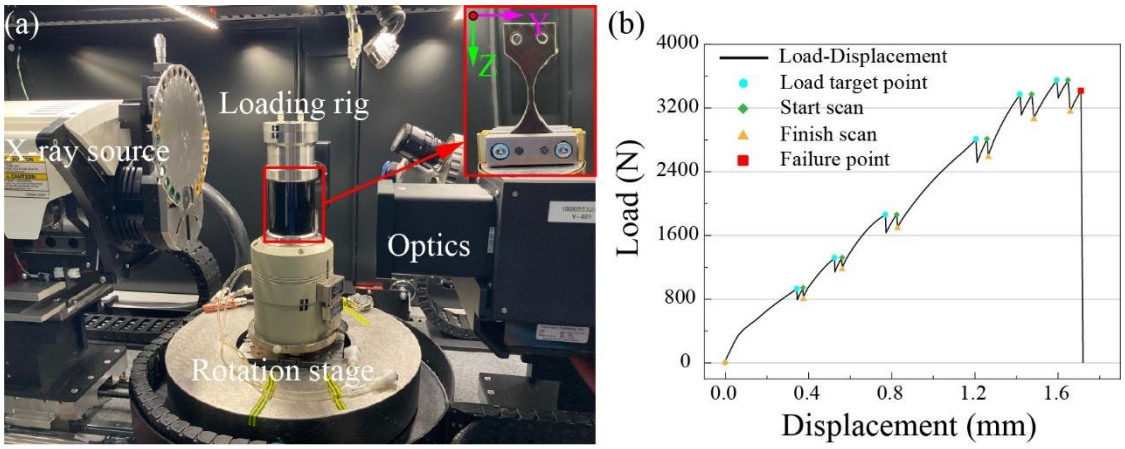

Figure 2: Experimental setup: (a) in-situ XCT tensile loading rig and close-up view of the specimen inside the support tube, and (b) tensile curve during the in-situ test

The experimental procedure involved sequentially applying predefined load increments (Table 1), holding the specimen at each load level for approximately 10 minutes after reaching the load target point (Figure 2 (b)) to achieve mechanical stability. During these 10 minutes, the controller adjusts the displacement to maintain the required load level. Following stabilisation, a tomography scan of the region of interest (ROI) is conducted, starting at the start scan point (Figure 2 (b)). The process of load application, settling, and scanning was systematically automated and repeated for six consecutive load steps. This relatively high frequency of loading steps and scans, unusual compared to those reported in the literature, was selected to ensure successful post-test correlation of the images for DVC analysis. For imaging, 1601 two-dimensional projection images were captured per

scan with an exposure time of 1 second per projection to minimise noise. For these scans, the X-ray source was set to a voltage of 150 kV and a power of 23 W. A 0.4× objective lens was selected, providing a 11.37 mm × 11.61 mm FOV, resulting in an isotropic voxel size of 11.34 μm. The captured projection images were reconstructed into three-dimensional volumes using the XMReconstructor software from ZEISS and a filtered back-projection algorithm, and saved as 16-bit datasets.

Two reference scans without any applied load (denoted as step 0 in Table 1) were first conducted to quantify DVC errors related to the correlation algorithm. Subsequently, the specimen was progressively loaded though displacement-control at a rate of 0.5 mm/min until each targeted load step was reached. These predefined load steps, detailed in Table 1, correspond to specific percentages of the ultimate tensile stress (UTS), expressed as the stress-to-failure ratio (SFR, σ/σ_{UTS}). The total duration to complete all scans across six load steps was approximately 9 hours.

Table 1: Load steps for the in-situ tensile test

Step	0	1	2	3	4	5	6
σ/σ_{UTS}	0	25%	37%	50%	75%	90%	95%
Load (kN)	0	0.93	1.31	1.86	2.8	3.36	3.54
Stress (MPa)	0	98	139	197	297	356	375

2.3 Digital Volume Correlation analysis

2.3.1 Data preparation

Each tomography scan was initially converted to an 8-bit dataset using the Avizo software [13] to reduce computational requirements for subsequent DVC analyses. The original XCT image volume had a size of 1003 × 1024 × 1009 voxels. Image thresholding was then applied to remove air-noise regions, resulting in well-defined Volumes of Interest (VOI), covering the entire gauge region of the specimen to enable reliable calculation of internal displacement and strain fields.

Prior to the correlation process, rigid body translations and rotations, inevitably introduced during specimen mounting and loading [11], were corrected using Avizo's image register module. Following the pre-registration procedure, the deformed volume was resampled using a Lanczos interpolation algorithm to exactly match the reference scan in both size and spatial position. The final aligned VOI used for DVC analysis had a size of 500 × 510 × 790 voxels.

2.3.2 DVC procedure and parameters

DVC algorithms are typically categorised into two approaches: sub-volume based (local) or finite element (FE) based (global) methods [14]. The local method divides the VOI into smaller sub-volumes, performing correlation analysis independently within each sub-volume to determine the displacement at its centre. This procedure does not ensure continuity of the displacements after deformation and can lead to gaps or overlaps (Figure 3 (a)). Conversely, global methods execute correlation across the entire VOI by deforming

a FE mesh and calculating nodal displacements, thus ensuring displacement continuity throughout the analysed volume [15] (Figure 3 (b)). Generally, local DVC (L-DVC) algorithms offer faster computation but may exhibit reduced accuracy, particularly for materials with poor internal texture. Global DVC (G-DVC), while computationally more demanding due to higher degrees of freedom, generally yields more robust and accurate displacement and strain results [9].

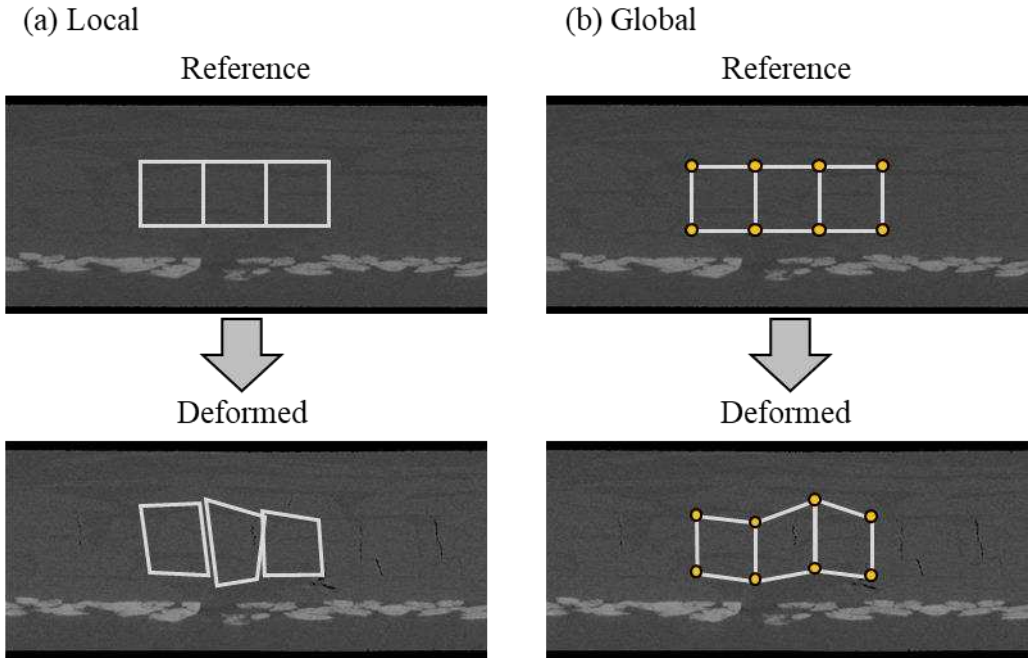

Figure 3: Schematic diagram illustrating the principle of (a) local DVC and (b) global DVC

In this study, the DVC analysis was performed using the XDigitalVolumeCorrelation module in the Avizo software [13]. A combined local-global DVC (LG-DVC) approach was selected to calculate internal displacement fields, based on previous established methods [16, 17]. This strategy initially uses a coarse displacement field obtained via L-

DVC to inform and guide the subsequent global solution, thus enhancing strain resolution, especially in complex deformation scenarios.

Initially, the L-DVC step uses a cross-correlation coefficient R_{L-DVC} to assess the similarity of two sub-volumes from reference and deformed images [18]:

$$R_{L-DVC}(x,y,z) = \frac{\sum\left(f_{sub}(x,y,z)g_{sub}(x^*,y^*,z^*)\right)}{\sqrt{\sum f_{sub}(x,y,z)^2 \sum g_{sub}(x^*,y^*,z^*)^2}} \tag{2.1}$$

where $f_{sub}(x,y,z)$ and $g_{sub}(x^*,y^*,z^*)$ represent the greyscale values in corresponding sub-volumes within the reference and deformed images, respectively. Values of R_{L-DVC} approaching unity indicate high similarity.

To ensure displacement continuity and accurate deformation fields throughout the entire volume, the G-DVC step is subsequently carried out. The quality of global correlation is assessed through the residual R_{G-DVC}, defined as [18]:

$$R_{G-DVC}(x,y,z) = f(x,y,z) - g(x^*,y^*,z^*) \tag{2.2}$$

where f and g represent the overall greyscale values inside image volumes. Smaller values of R_{G-DVC} indicate higher accuracy for the correlation.

For LG-DVC analysis, relatively large sub-volumes are initially used for the L-DVC step to obtain preliminary coarse displacement fields, which are then used as boundary conditions for a subsequent refined G-DVC analysis. For the G-DVC step, an unstructured finite element mesh consisting of four-noded tetrahedral grids was generated based on the specimen geometry. The G-DVC procedure was conducted using a maximum of 500 iterations and a convergence criterion of 0.001.

Incremental displacement fields obtained from the LG-DVC analysis between consecutive load steps are cumulatively summed to derive the total displacement fields at each loading stage with reference to the undeformed configuration.

2.4 Strain calculations

2.4.1 Macroscopic strain calculation

To establish the macroscopic mechanical response of the TFP composite specimen, the global axial strain (along the loading direction) was calculated from the average of axial displacement values measured along two opposite surfaces delimiting the specimen's gauge length region. The global axial strain ε was computed as:

$$\varepsilon = \frac{D_{z,top} - D_{z,bot}}{H_{z,top} - H_{z,bot}} \tag{2.3}$$

where $D_{z,top}$ and $D_{z,bot}$ represent averaged axial displacements along the top and bottom surfaces, respectively, and $H_{z,top} - H_{z,bot}$ is the initial gauge length.

2.4.2 Local strain calculation

Displacement fields obtained from the DVC analysis were used to compute the deformation gradient and subsequently the corresponding Green-Lagrange strain tensor components [19], for detailed internal deformation analysis. The maximum principal strain was also extracted from the strain tensor results since it is a commonly used critical parameter for tracking crack initiation and early damage evolution within complex composite microstructures [20].

2.4.3 Strain transformation

In addition, directional local strain components relative to specific fibre orientations within each ply were evaluated to analyse the local anisotropic response in relation to crack formation.

Global strain components were therefore transformed into directional strain components related to fibre orientations within each ply via a standard tensor rotation procedure [21]. The coordinate system defines the X-axis as the through-thickness direction (consistent with Figure 1), the Z-axis as the loading direction, and the Y-axis as the transverse direction of the specimen (Figure 2 (a)). Under this defined coordinate system, directional strain components are evaluated by rotating the global coordinate system about the X-axis by an angle θ_r, which represents the inclination of the fibre direction relative to the Z-axis within the YZ plane. For example, a ±60° off-axis fibre orientation corresponds to θ_r=±60°. This systematic rotation enables the extraction of strain components aligned with the fibre direction, as well as the transverse and through-thickness directions.

The directional strain ($\boldsymbol{\varepsilon}'$) in the transformed coordinate system (x', y', z') can thus be expressed using the original global strain tensor ($\boldsymbol{\varepsilon}$) via the strain transformation matrix [T_ε] [21]:

$$\boldsymbol{\varepsilon}' = [T_\varepsilon]\boldsymbol{\varepsilon} \tag{2.4}$$

where:

$$\boldsymbol{\varepsilon}' = \left[\varepsilon'_{xx}, \varepsilon'_{yy}, \varepsilon'_{zz}, \gamma'_{yz}, \gamma'_{xz}, \gamma'_{xy}\right]^T, \boldsymbol{\varepsilon} = \left[\varepsilon_x, \varepsilon_{yy}, \varepsilon_{zz}, \gamma_{yz}, \gamma_{xz}, \gamma_{xy}\right]^T$$

and the transformation matrix for rotation about the X-axis by angle θ_r is defined as [21]:

$$[T_\varepsilon] = \begin{bmatrix} 1 & 0 & 0 & 0 & 0 & 0 \\ 0 & c_r^2 & s_r^2 & c_r s_r & 0 & 0 \\ 0 & s_r^2 & c_r^2 & -c_r s_r & 0 & 0 \\ 0 & -2c_r s_r & 2c_r s_r & c_r^2 - s_r^2 & 0 & 0 \\ 0 & 0 & 0 & 0 & c_r & -s_r \\ 0 & 0 & 0 & 0 & s_r & c_r \end{bmatrix} \quad (2.5)$$

with:

$$c_r = \cos\theta_r \, , s_r = \sin\theta_r \quad (2.6)$$

This systematic transformation enables the extraction of strain values along fibre, transverse, and through-thickness directions, providing a more comprehensive basis for interpreting damage initiation and propagation in anisotropic composite materials.

2.5 DVC uncertainty measurements

To evaluate the robustness of the LG-DVC strategy, a sensitivity analysis was conducted to assess the influence of the sub-volume size used in the initial L-DVC step on the final computed displacement fields. This was performed using two repeated, unloaded scans of the specimen, allowing the analysis of DVC uncertainty under zero-strain conditions. The isotropic sub-volume size (i.e., cubic sub-volumes with equal edge lengths in all three directions) was varied from 21 to 111 voxels in increments of 10 voxels using the DVC Uncertainty Measurement module in the Avizo software.

Based on these reference volumes, the accuracy and precision of the LG-DVC procedure were further quantified by calculating the mean and standard deviation of the computed strain component values. The evaluation was performed using all three directional strain components (ε_{xx} , ε_{yy}, ε_{zz}) as well as the corresponding normal-directional displacements. This analysis enabled the identification of an optimal sub-volume size that provided a

balance between correlation accuracy and spatial resolution, ensuring reliable input fields for subsequent G-DVC analysis.

2.6 Crack and microstructural segmentation

The fibre bundle structure was segmented from the XCT image volumes using a threshold-based method combined with morphological filtering. This was done to facilitate the visualisation of the spatial correlation between fibre bundle arrangements, strain localisation patterns, and the subsequent initiation and development of cracks.

The image segmentation procedure for extracting and analysing crack distributions is illustrated in Figure 4, using the XCT result from load step 4 as an example. As shown in Figure 4 (a), the original XCT image volume clearly revealed the presence of edge cracks induced by tensile loading. In order to isolate cracks from the surrounding material, an intensity-based thresholding method was initially applied using Avizo's interactive thresholding module, resulting in a low-density phase containing both crack information and noise-related voxels (Figure 4 (b) and (c)). To further eliminate isolated noise-related voxels, a voxel-based filtering process was performed using the "Remove Small Spots" function in Avizo. A minimum voxel cluster size of 80 voxels was set, ensuring that only larger, connected clusters corresponding to actual cracks were retained (Figure 4 (d)). The final segmented cracks were subsequently used for quantitative analysis of crack distributions and morphological characteristics.

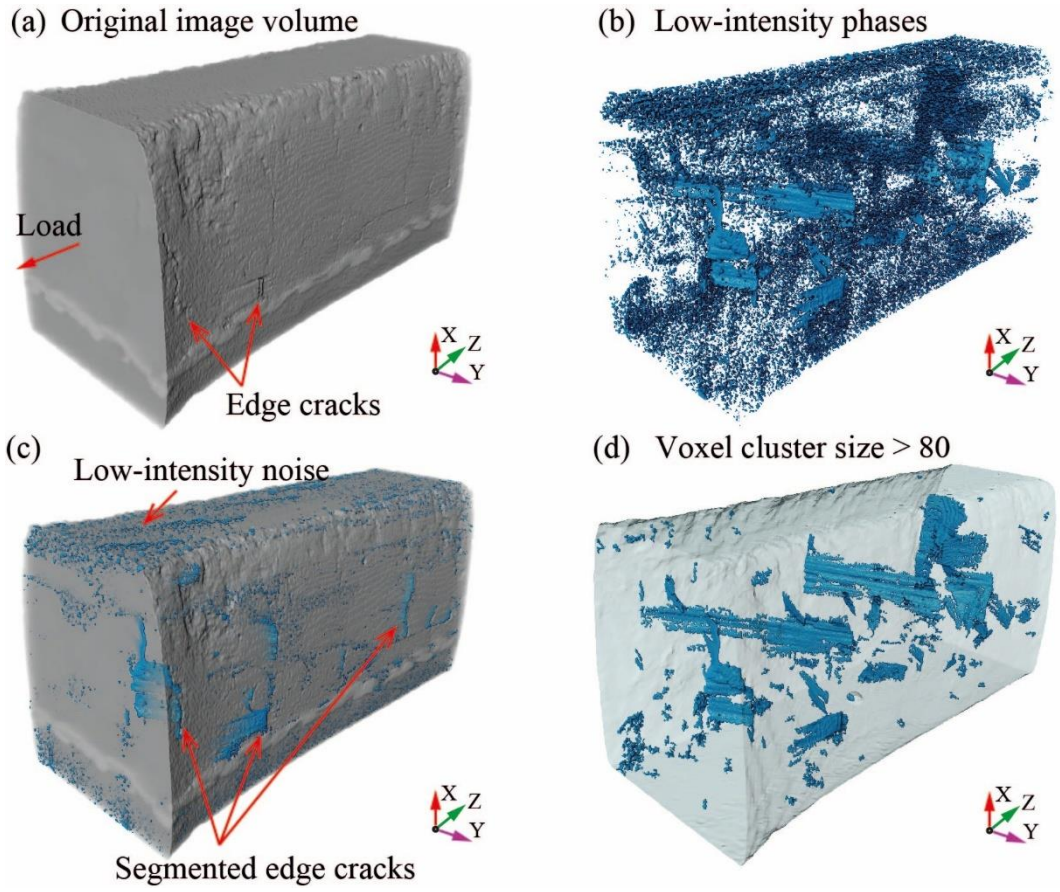

Figure 4: Cracks segmentation for step 4: (a) original image volume showing cracks at the sample's edge; (b) initial thresholding capturing all low-intensity phases, including both cracks and noise; (c) overlay of segmented cracks and noise on the original volume; (d) final filtered cracks retaining only voxel clusters larger than 80 voxels

3 Results

3.1 Crack initiation and propagation

3.1.1 Crack morphology

The 3D crack morphology evolution from initial crack formation at 50% σ_{UTS} to off-axis crack accumulation and interlaminar delamination seen at 95% σ_{UTS} is shown in

Figure 5 along with 2D cross sections of the internal TFP composite structure at the mesoscale.

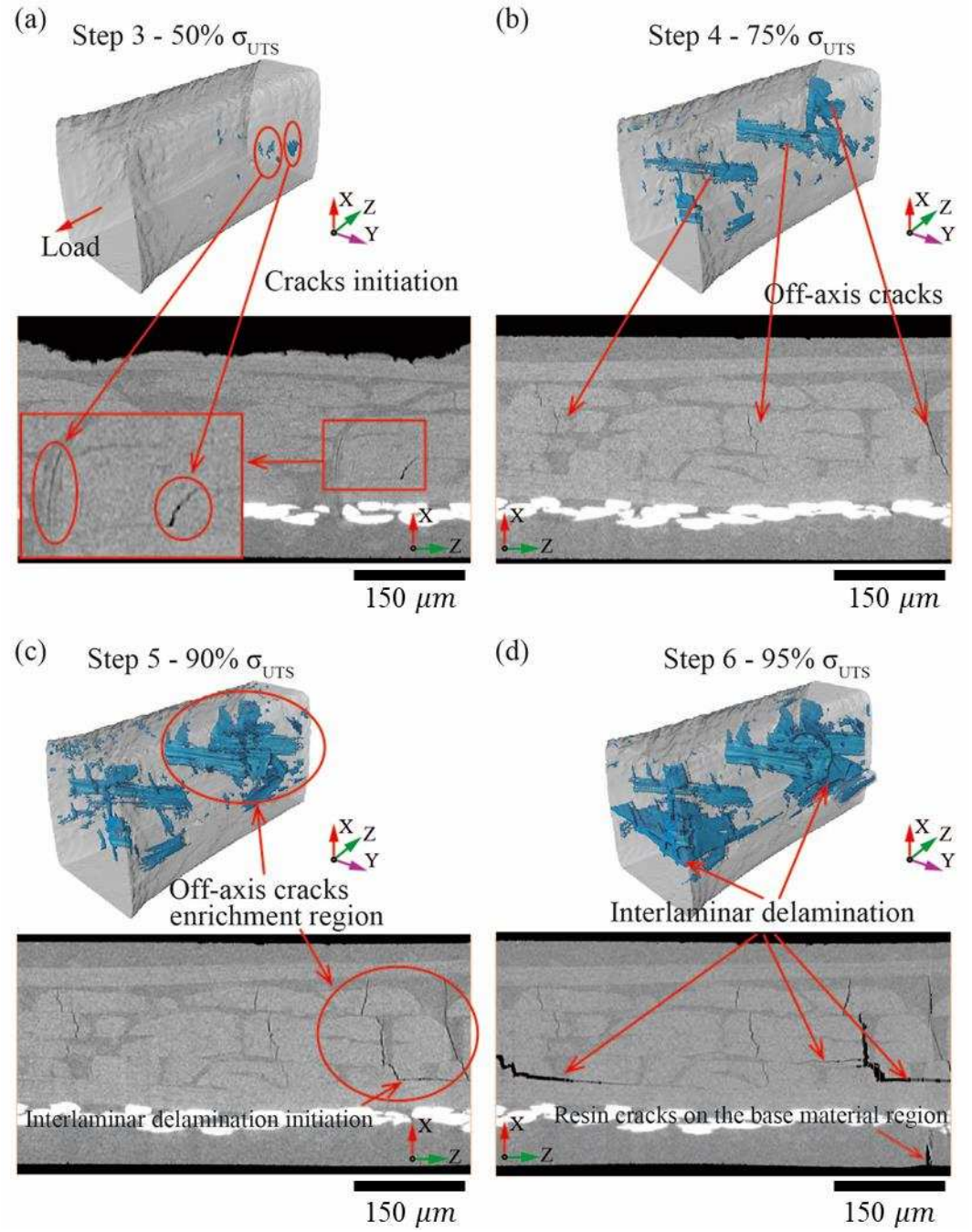

Figure 5: 3D evolution of crack morphology for stress-to-failure ratio from 50% to 95% σ_{UTS}. 3D segmented cracks (top row) are visualised alongside corresponding 2D cross-sectional XCT images (bottom row). (a) Initial cracks at 50% σ_{UTS}, including

isolated cracks near stitching threads (highlighted by the red ellipse) and within fibre bundles; (b) Crack propagation and formation of off-axis cracks at 75% σ_{UTS}; (c) Expansion of off-axis cracks and onset of interlaminar delamination at 90% σ_{UTS}; (d) Extensive interlaminar delamination and cracks within resin-rich regions near the base material at 95% σ_{UTS}

No visible cracks were detected from step 0 (0% σ_{UTS}) through to step 2 (37% σ_{UTS}). At step 3 (50% σ_{UTS}), cracks initiated primarily at the specimen's edge surface within layer 5 (60°). Isolated cracks were also identified within stitching threads adjacent to fibre bundles in layers 3 and 4, as indicated by the red ellipse in Figure 5 (a). Between step 3 (50% σ_{UTS}) and step 4 (75% σ_{UTS}), the crack density markedly increased. While initial cracks had formed in layer 5, significant crack propagation occurred predominantly in layers 3 and 4 along the -60° off-axis directions, with minimal further growth observed in layer 5. At step 5 (90% σ_{UTS}), extensive off-axis crack development is observed in the ±60° plies, with several cracks traversing from one specimen's edge to the opposite edge. Notably, one significant -60° off-axis crack propagated from layer 3 (-60°) through layer 4 (-60°) into layer 5 (60°), inducing the first interlaminar delamination between layers 5 (60°) and 6 (0°), as pointed by the red arrow in Figure 5 (c).

At the final loading step (step 6, 95% σ_{UTS}), substantial crack volume expansion occurred (Figure 5 (d)). Dominant cracks remained oriented off-axis (±60°), but longitudinal cracks in the 0° direction became increasingly pronounced, particularly in layer 6, with minor crack formation in layer 1. The cracks observed at this stage were extensively

interconnected with larger interlaminar delamination regions, primarily situated between layers 5 (60°) and 6 (0°). Additionally, at the bottom of the specimen, a significant matrix crack formed within the matrix-rich region adjacent to the base material, coinciding with the final stage of damage evolution.

A more detailed analysis of early-stage crack formation reveals that cracks initiated at the edge of layer 5 rather than within the mid-thickness plies (layers 3 and 4). Two off-axis cracks were detected within the fibre bundle of layer 5, while matrix cracks emerged in the resin-rich regions at the opposite specimen's edge (zones A and B respectively in Figure 6). The matrix cracks in the resin-rich regions propagated through the thickness and were observed to develop within the stitching threads, indicating that the stitching regions may act as preferred sites for early crack formation.

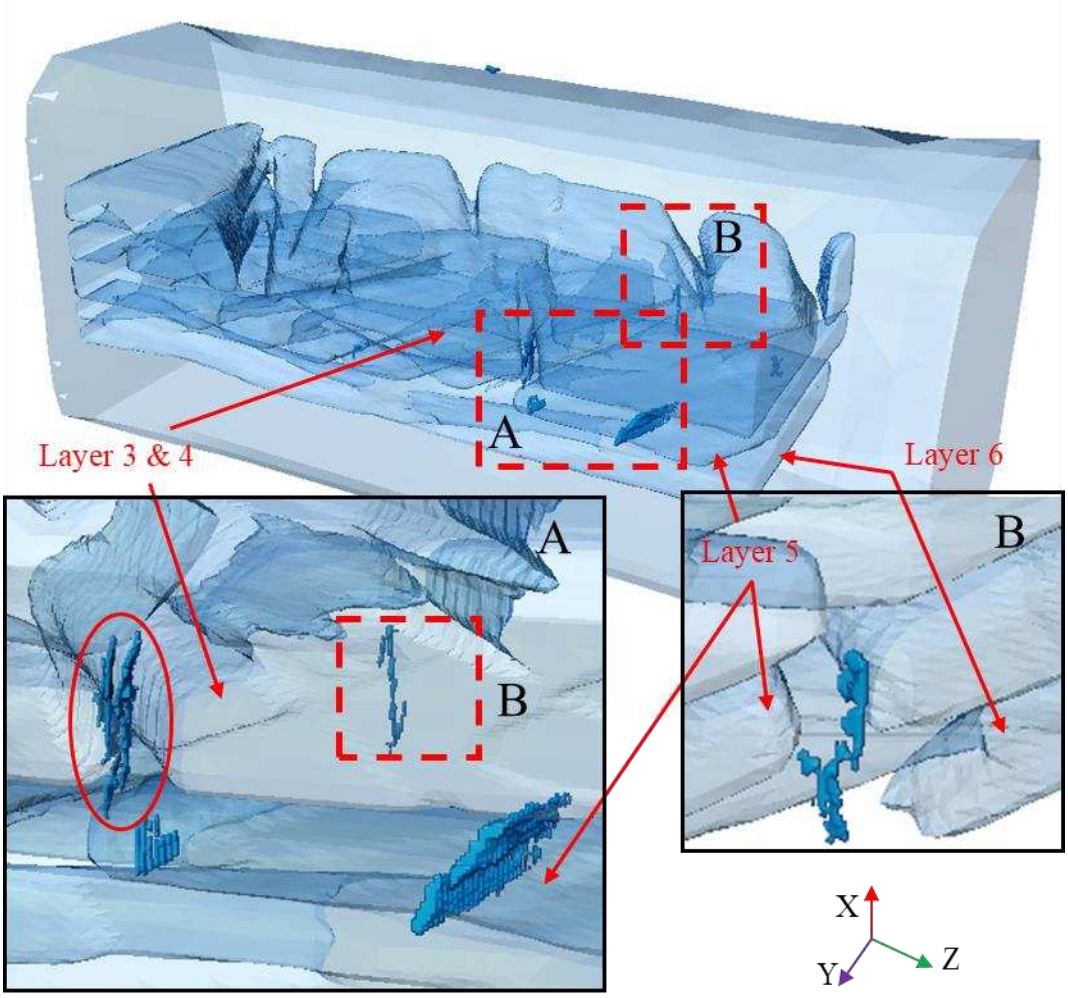

Figure 6: Cracks (dark blue) initiation and interaction with fibre bundle structures (step 3, 50% σ_{UTS})

With further loading, off-axis cracks became prominent in layers 3 and 4, where they propagated laterally along the fibre tow direction from one edge of the specimen to the other (red ellipse, Figure 7). In contrast, the cracks initially formed in layer 5 (green ellipses, Figure 7) and within the resin-rich zones (zone B) showed limited propagation. Only the crack which initiated in the resin-rich zones of zone A (red ellipse, Figure 6 and 7) appeared to link with the larger off-axis cracks in the adjacent plies (layers 3 and 4).

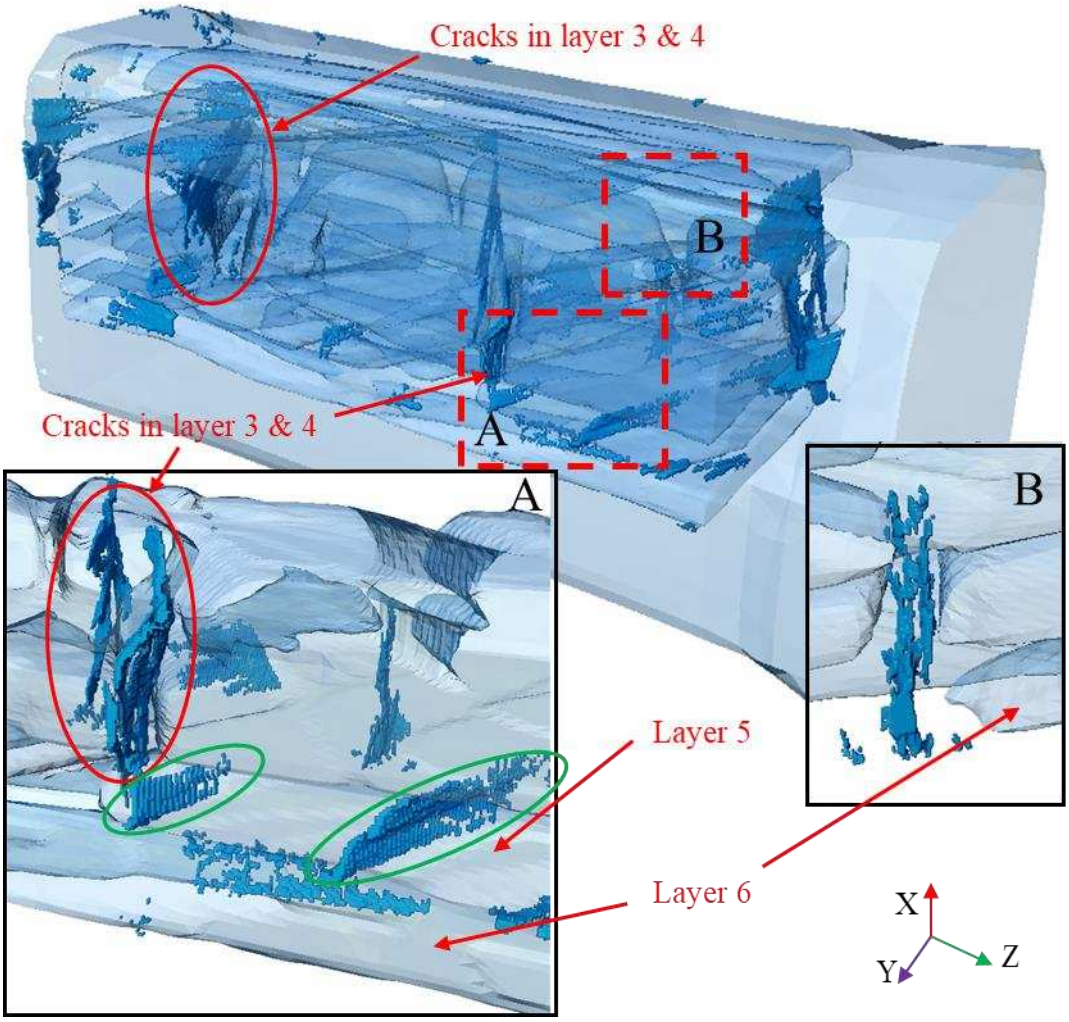

Figure 7: Cracks propagation and its interaction with fibre bundle structures (step 4, 75% σ_{UTS})

3.1.2 Quantitative analysis of crack propagation

Crack volumes were quantitatively determined from the segmented XCT data using a voxel-counting method. The results at each loading step are presented in Figure 8. No cracks were detected up to step 2 (37% σ_{UTS}), and only a minimal volume was recorded at step 3 (50% σ_{UTS}), corresponding to the onset of damage. A notable increase in crack volume occurred between step 3 and step 4 (50% to 75% σ_{UTS}), indicating early-stage

damage accumulation. This trend continued from step 4 to step 5 (75% to 90% σ_{UTS}) with sustained crack propagation and the onset of interlaminar delamination.

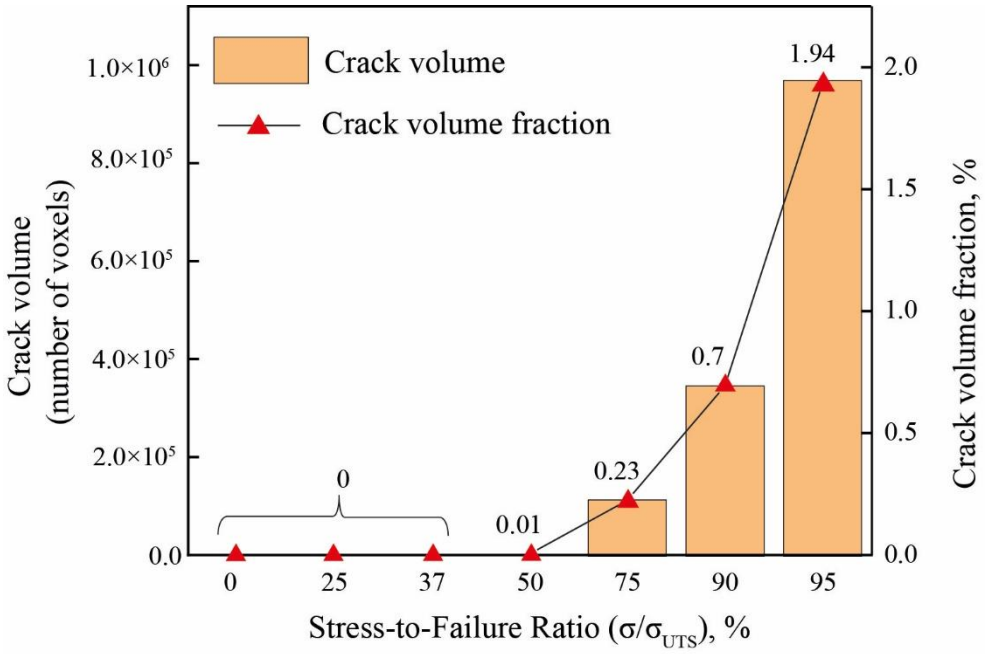

Figure 8: Evolution of crack volume and crack volume fraction with respect to the stress-to-failure ratio (σ/σ_{UTS})

The most pronounced change was observed between step 5 and 6 (90% to 95% σ_{UTS}), where the crack volume nearly tripled despite only a 5% increase in the stress-to-failure ratio. This sharp rise suggests a transition from stable crack growth to unstable, rapid damage propagation, characteristic of imminent catastrophic failure. Overall, the quantitative data indicate that while initial damage developed gradually beyond 50% σ_{UTS}, the final failure process was dominated by rapid crack expansion in the last stages of loading.

3.2 Digital Volume Correlation analysis

3.2.1 Uncertainty measurement

Measurement uncertainty and sensitivity of the LG-DVC approach was evaluated by correlating two consecutive XCT reference scans without loading. Figure 9 shows the effect of the sub-volume size used in the L-DVC method on the calculated mean and standard deviation of displacement and strain values. The sub-volume size varied incrementally from 21 voxels to 111 voxels, with an increment step of 10 voxels.

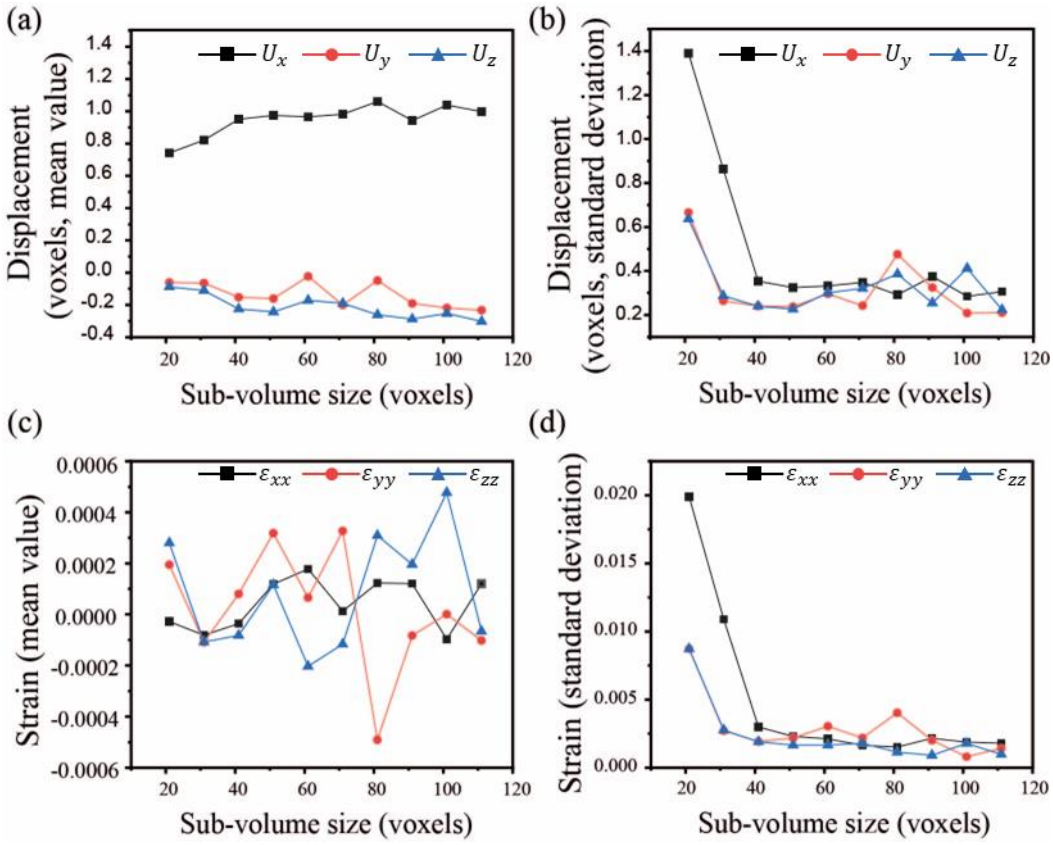

Figure 9: Effect of sub-volume size (voxels) on displacement and strain measurement uncertainty: (a) mean value and (b) standard deviation of displacement components, (c) mean value and (d) standard deviation of strain components

Figure 9 (a) shows mean displacement values along the x-, y-, and z-directions. The displacement along the x-direction exhibits higher values compared to the y- and z-directions, initially increasing from about 0.5 voxel for a 21-voxel sub-volume size to about 1 voxel for a 41-voxel sub-volume size, after which it stabilises around 1 voxel. In contrast, displacements along the y- and z-directions remained consistently low, stabilising at approximately -0.2 voxel and -0.3 voxel, respectively. Corresponding mean strain values are negligible for all tested sub-volume sizes, remaining consistently near a zero value (Figure 9 (c)).

The standard deviation of the displacement fields (Figure 9 (b)) notably decreases with increasing the sub-volume size, indicating improved precision. A similar trend is observed for the strain standard deviations (Figure 9 (d)), which also decrease rapidly as the sub-volume size increases. However, for excessively large sub-volume sizes (>71 voxels), a slight increase in the strain standard deviation is observed, suggesting a loss in measurement precision for overly large sub-volume.

Based on this sensitivity analysis, a sub-volume size of 51 voxels was selected for subsequent L-DVC analysis. Using this setting as the initial condition for the G-DVC procedure with a grid size of 32 voxels, convergence was reached after 253 iterations. The resultant standard deviation of displacement components was 0.11, 0.03, and 0.04 voxel along the x-, y-, and z-directions, respectively. Correspondingly, mean strain values were $5.88\times10^{-4}\ \mu\epsilon$, $-4.65\times10^{-4}\ \mu\epsilon$, and $6.27\times10^{-4}\ \mu\epsilon$, with standard deviation values of 1.25×10^{-3}, 2.69×10^{-4}, and 3.13×10^{-4} along the x-, y-, and z-directions, respectively. Thus,

the DVC analysis procedure combining the local and global methods demonstrated minimal noise in measuring the 3D deformation and strain fields, confirming the accuracy and precision of results.

3.2.2 Overall mechanical response

The macroscopic stress-strain response of the TFP composite under uniaxial tensile loading is shown in Figure 10. A relatively linear relationship is observed up to step 5, indicating predominantly elastic deformation behaviour. The calculated tensile modulus was approximately 32 GPa. For the final loading step (step 6), deviation from linearity is observed, coinciding with the onset of pronounced cracking and delamination captured in the XCT-based crack analysis (Figure 5 (d)).

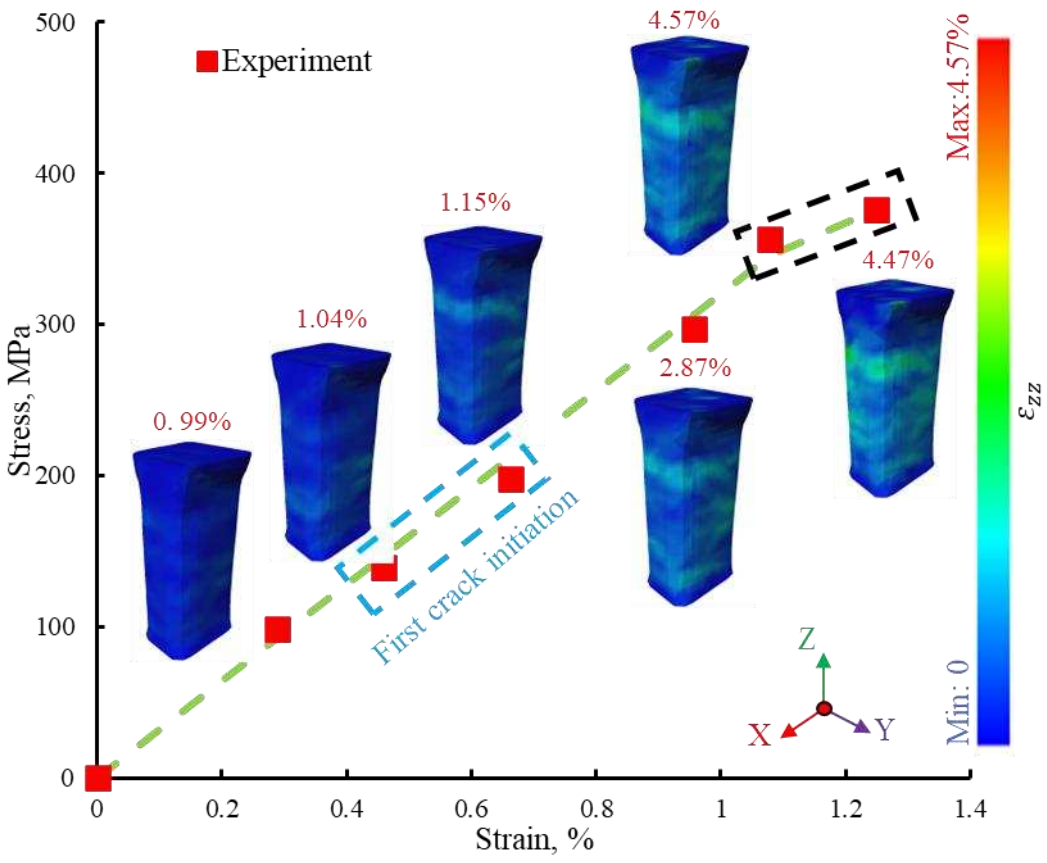

Figure 10: Macroscopic stress-strain response of the TFP composite derived from DVC-based displacement measurements. Strain maps show ε_{zz} distributions overlaid on 3D VOIs at selected loading steps, aligned with experimental stress-strain data (red squares). A unified strain colour scale is used across all maps to enable comparison of strain evolution

The full field z-directional strain (ε_{zz}) maps at each correlation step are depicted from volumetric strain fields, visualised through representative 3D VOI in Figure 10, with the maximum local strain value reported in red at the top of each map. These strain maps provide a clear visualisation of strain distribution throughout the loading process and highlight the heterogeneity of deformation in the TFP composite under tensile loading, with maximum local strain values much higher than the macroscopic strain results. The heterogeneity is attributed to the internal geometric irregularities, e.g. resin/tow interfaces, stitching threads, resin-rich zones and fibre waviness.

3.2.3 Influence of layup sequence and TFP architecture on strain distribution

To further understand the observed local strain localisation and its correlation with the internal structure, the layer-wise strain distribution was examined. Although the maximum principal strain field identifies the most critical regions of crack initiation, the directional strain component ε_{xx} provides insight into how the unique TFP layup and stitching configuration affect local deformation prior to failure.

Figure 11 shows the ε_{xx} strain distribution obtained from the DVC results between step 0 and step 1. The strain values were extracted along a probe line (red dashed line in Figure

11 (a)) positioned through the middle region of the specimen. The strain profile was plotted along the through-thickness direction. Negative strain values were expected due to Poisson contraction under axial tensile loading.

The ε_{xx} distribution showed a clear asymmetry, with the maximum compressive strain value located slightly off the specimen mid-thickness plane (Figure 11 (b)), within layer 5. These observations were confirmed by overlaying the strain maps on the segmented fibre bundle structure (Figure 11 (a)), which highlighted the relationship between localised deformation and internal architectural features.

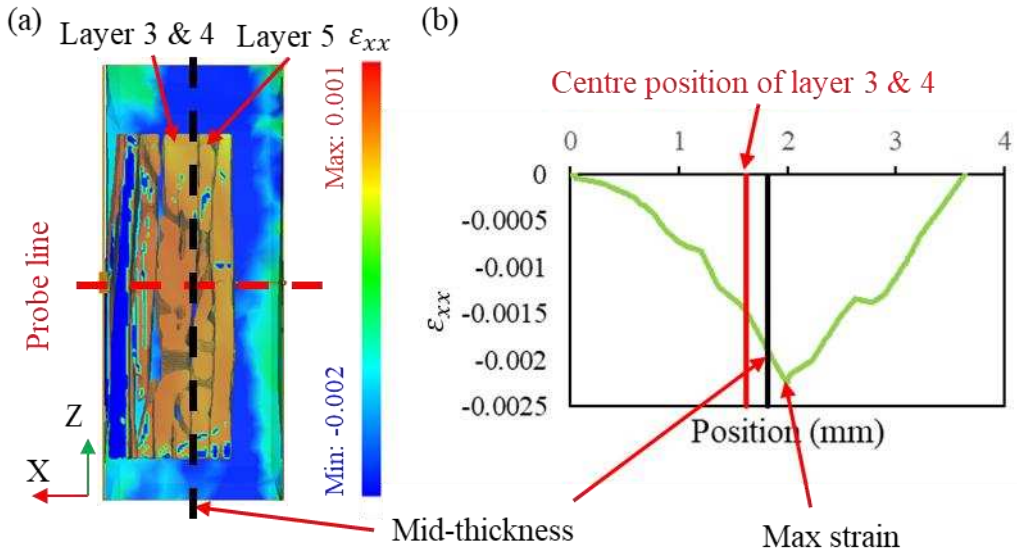

Figure 11: Through-thickness ε_{xx} strain distribution for the correlation step 0-1: (a) 2D strain map with superimposed segmented fibre bundle structure, (b) ε_{xx} strain profile extracted along a central probe line in (a) through the thickness direction (X-axis)

3.2.4 Strain distributions for damage analysis

The full-field maximum principal strain maps generated at each loading step, which are instrumental for the analysis of potential strain concentrations possibly related to initial

microcrack formation are shown in Figure 12. At 25% SFR (correlation between steps 0 and 1), ε_1 remains relatively low (0.01) and uniformly distributed in the gauge region of the specimen. Prior to crack initiation (50% SFR, Figure 5 (a)), at 37% SFR (correlation between steps 0 and 2), while the maximum 1st principal strain value remains low (0.011), a strain concentration can be found in the middle region of the gauge length, located in the base material, which contains mainly glass fibres, resin and stitching threads. More evidence of strain concentration can be found at 50% SFR (correlation between steps 0 and 3), within the same region as in the previous loading step, but also at another location found at the transition between the shoulder of the specimen and the gauge length (red dashed box), indicating the region of appearance of the first crack (see Figure 5 (a)).

A rapid increase in strain magnitude was observed between steps 3 (maximum ε_1 = 0.012) and 4 (maximum ε_1 = 0.066, Figure 12 (d)), clearly reflecting significant local damage progression or crack-related deformation. However, despite higher global loading for subsequent correlation steps (0-5, 0-6), the maximum ε_1 values decreased (0.062 for 0-5 and 0.054 for 0-6, Figure 12 (e) and (f), respectively). It should be noted that such a decrease in maximum 1st principal strain values for latter loading steps, when widespread cracks and delamination occur, might be related to local DVC artefacts or difficulties in accurately resolving strain values in highly damaged regions, where significant greyscale decorrelation and local discontinuities are present [19, 22]. Nevertheless, the strain maps since step 3 show consistently intensifying bands of deformation (red-dashed box in Figure 12 (c)) coinciding with locations of crack formation. The strain map at step 0-6

reveals another extensive band-shaped ε_1 concentration between plies (red-dashed boxes in Figure 12 (f)), spatially coincident with the interlaminar delamination zone identified in Figure 5 (d), further confirming that inter-ply damage appears at a late stage of deformation of the TFP laminate.

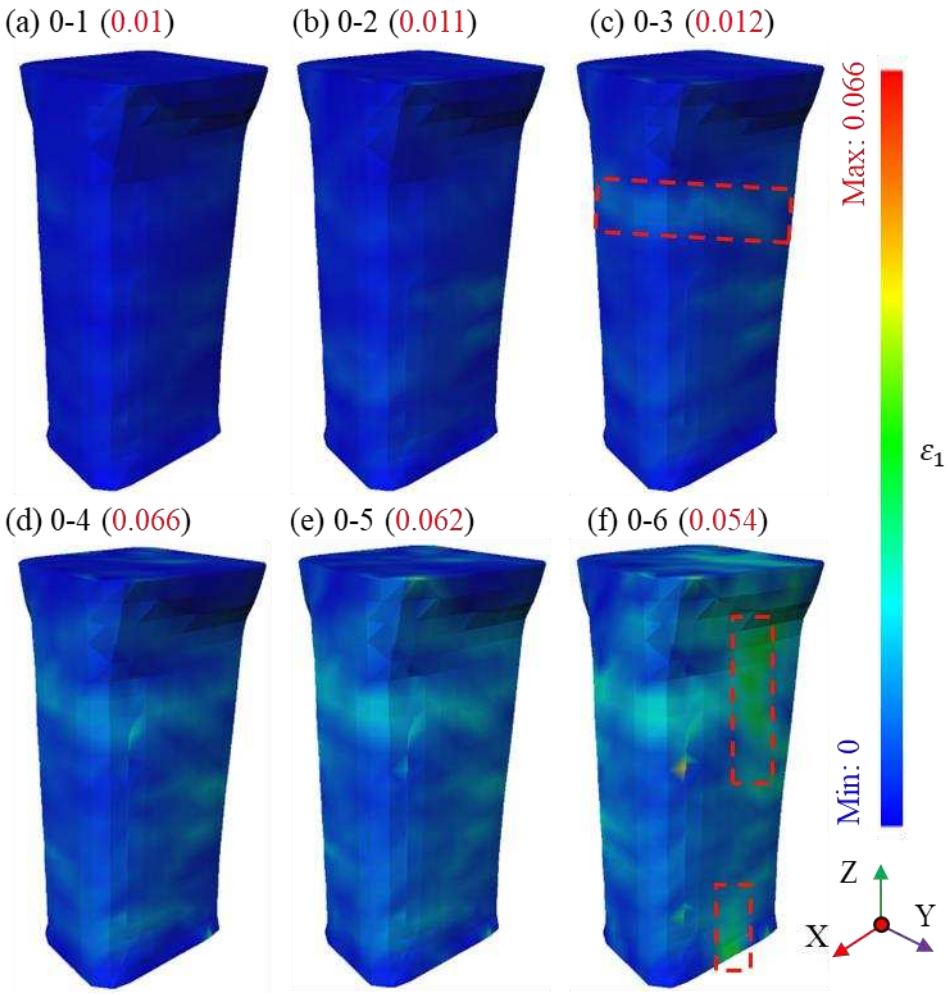

Figure 12: 3D visualisation of maximum principal strain (ε_1) evolution in the TFP composite for each DVC correlation step with respect to the undeformed image. A unified strain colour scale from 0 (blue) to 0.066 (red) is applied to enable direct comparison of strain distribution across steps. The maximum local strain value is indicated in brackets and red dashed boxes show areas of strain concentrations

To further analyse damage initiation, the local strain ε'_z (fibre-parallel) and ε'_y (fibre-transverse) fields (equations 2.4-2.6) rotated by θ_r=±60° about the X-axis (through-thickness direction) for layers 3 and 4 (Group A, θ_r=-60° with respect to the tensile direction), layer 2 (Group B, θ_r=+60°) and layer 5 (Group C, θ_r=+60°) are shown in Figure 13, plotted onto the fibre bundles of the plies. Two components are shown for each group: the fibre-parallel strain (a-c), ε'_z, and the fibre-transverse strain (d-f), ε'_y, which describe the axial and transverse responses of the off-axis bundles, respectively. Different colour scale ranges are used for distinct volumetric strain fields to better visualise strain concentrations in the various plies. The maximum and minimum strain values are shown above and below the volumetric strain fields, with red colour for maximum value and blue colour for minimum value, respectively, corresponding to the colour bar. Maps are provided for three consecutive loading steps with reference to the undeformed configuration (0-1, 0-2, and 0-3, corresponding to (a-c) and (d-f)), capturing the strain evolution leading up to and including the onset of crack initiation at step 3 (Figure 5 (a)). In layers 3 and 4 (Group A of Figure 13), as the nominal middle layers of the TFP composite with layup sequence of $[0/60/-60]_s$, both ε'_y and ε'_z increase monotonically, with their peak values rising from 1.2e-3 to 3.6e-3 and from 2.9e-3 to 8.7e-3, respectively. The larger magnitudes of ε'_y highlight the greater transverse deformation experienced by the bundles, which arises from the lower resistance to deformation in the direction perpendicular to the fibres. For ε'_z, pronounced positive strain concentrations develop near the specimen edges whereas negative concentrations appear in the interior, reflecting

edge, constraints from other plies and Poisson effects. By contrast, ε'_y shows more uniform strain distributions with local concentrations at the edges eventually leading to a band of deformation in the region highlighted by the blue dashed box in Figure 13. It is worth noting that the strain concentration significantly shifts in step 0-3, with the highest strain of 8.7e-3 almost twice that of the maximum strain value in step 0-2 (Figure 13 (e)), to a band of concentrated deformation in a region where a crack first forms in layer 5 (Figure 5 (a)).

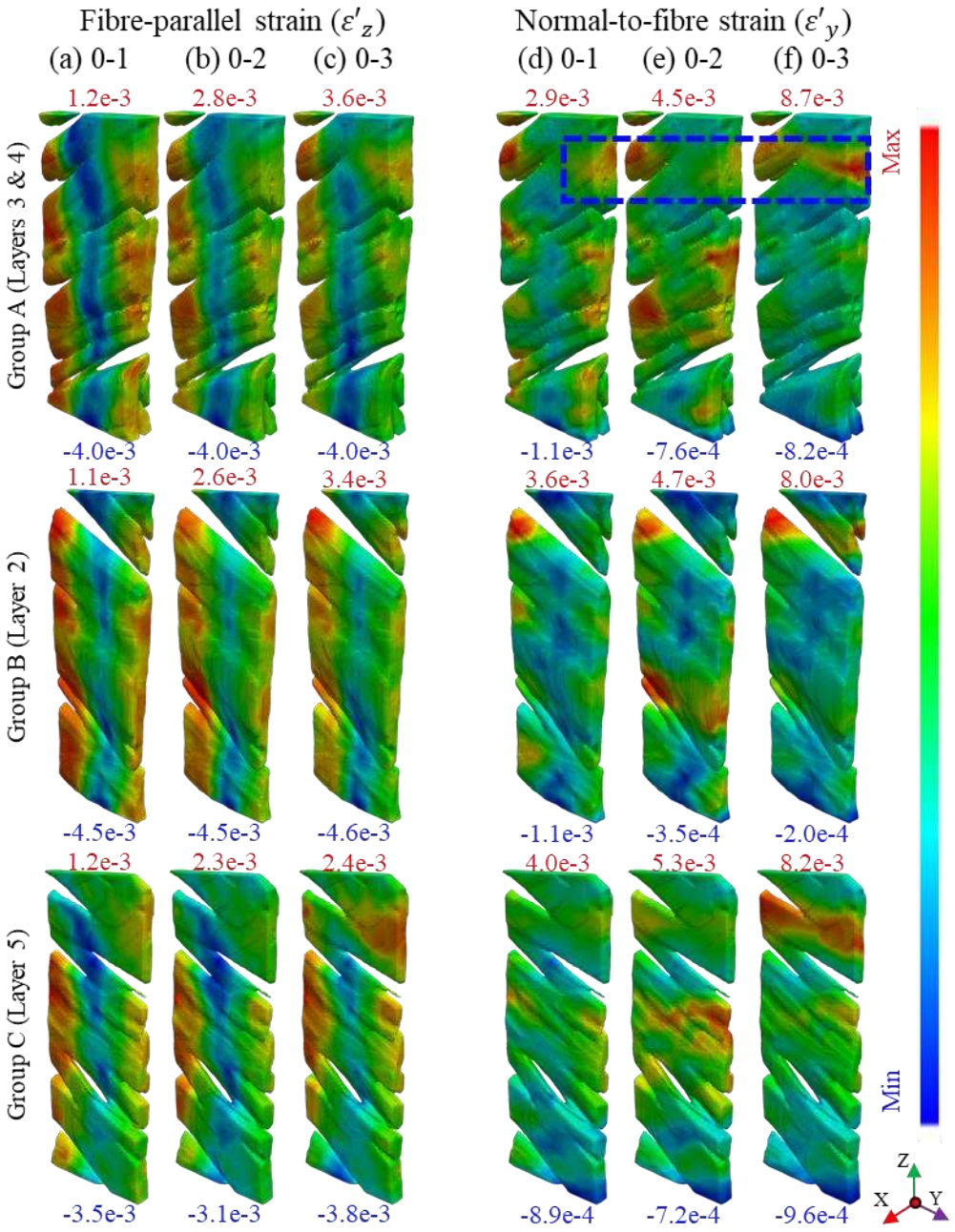

Figure 13: Rotated strain maps in segmented fibre bundles of layers 3 and 4 (-60°, Group A), layer 2 (60°, Group B), and layer 5 (60°, Group C), showing fibre-parallel strain ε'_z (a-c) and fibre-transverse strain ε'_y (d-f), corresponding to correlation steps 0-1, 0-2, 0-3

The rotated strain maps for layers 2 (Group B), and 5 (Group C) (+60° with respect to the global Z-axis) are shown in Figure 13. ε'_z results from both layers (Group B and C, (a-c)) exhibit similar distribution patterns to those observed in layers 3 and 4 (Group A, (a-c)), with positive strain values along the edges and mid-region negative strain values, reflecting sample edge, constraints from other plies and Poisson effects. For ε'_y in layer 2 (Group B, (d-f)), localised strain concentration is primarily at the edge of the specimen and near the boundary between fibre bundles and the resin-rich zones. The maximum ε'_y strain increases from 3.6e-3 to 8.0e-3 across the three steps. In contrast, ε'_y in layer 5 (Group C (d-f), Figure 13) shows a more pronounced strain concentration from the start with a higher strain value of 4.0e-3 at correlation step 0-1 (Group C (d)) compared to strain values in other layers (Group A (d) and B (d)). This is primarily caused by the layup architecture of the TFP composite that was discussed in the section 3.2.3. Transverse ε'_y concentration becomes more intense at correlation step 0-2 (Group C (e)) reaching 5.3e-3. Strain concentrations appear along the sample edge and in structurally complex regions near the mid-height (Z-axis) of the specimen, consistent with the stitched architecture visualised in the segmented geometry. At step 3, a significant spatial shift in strain concentration is observed with a localised high-strain band emerging near the top of the segmented model, and with values increasing markedly, reaching 8.2e-3 (Group C (f)). This concentration coincides spatially with the region where crack initiation was first detected in layer 5 (Figure 5 (a)) and aligns with the strain

intensification also observed in layers 3 and 4 (Group A), suggesting a structural linkage between fibre bundle architecture and localised failure.

Figure 14 shows strain maps for the 0° directional layers (layer 1, Group A; and layer 6, Group B), visualised consistently with the approach used in Figure 13. It should be noted that some regions in layer 1 (highlighted by the red dashed boxes in Group A) lie outside the DVC computation domain, resulting in artificially assigned zero strain values.

Distinct strain distributions are evident when compared to off-axis layers (Figure 13), for both fibre-parallel strain (ε'_z) and fibre-transverse strain (ε'_y), highlighting the effect of fibre orientation on the strain response in each ply of the laminate. The fibre-parallel strain (ε'_z) distributions in layers 1 and 6 show similar pattern, starting with strain concentrations at the edges of the layers at low applied load (step 0-1). As loading progresses, these concentrations evolve into clearly defined deformation bands (highlighted by black dashed boxes). Notably, at step 0-3, a pronounced band of highest strain magnitude (0.01) eventually crosses the entire width of the two layers in the region of the specimen where the first crack was located in layer 5. The strain magnitude within this band exceeds those recorded in other layers (see Figure 13). Given the inherent ply-to-ply interactions within the laminate structure, the emergence and progression of this deformation band in layers 1 and 6 might explain the shift in bands of strain localisation observed in layer 5 (see Figure 13 (e) and (f), Group C).

Regarding the fibre-transverse strain component (ε'_y), localisation is also evident near the edges of the specimen, although it does not develop into distinct deformation bands

extending across the layer width, as observed for the fibre-parallel strain. Nevertheless, a notable strain concentration appears in layer 6 (highlighted by the blue dashed box), corresponding spatially to the crack location in layer 5. Additionally, it should be emphasised that the ε'_y strain magnitudes recorded in layers 1 and 6 are significantly lower than those in the off-axis layers shown in Figure 13 for each loading increment.

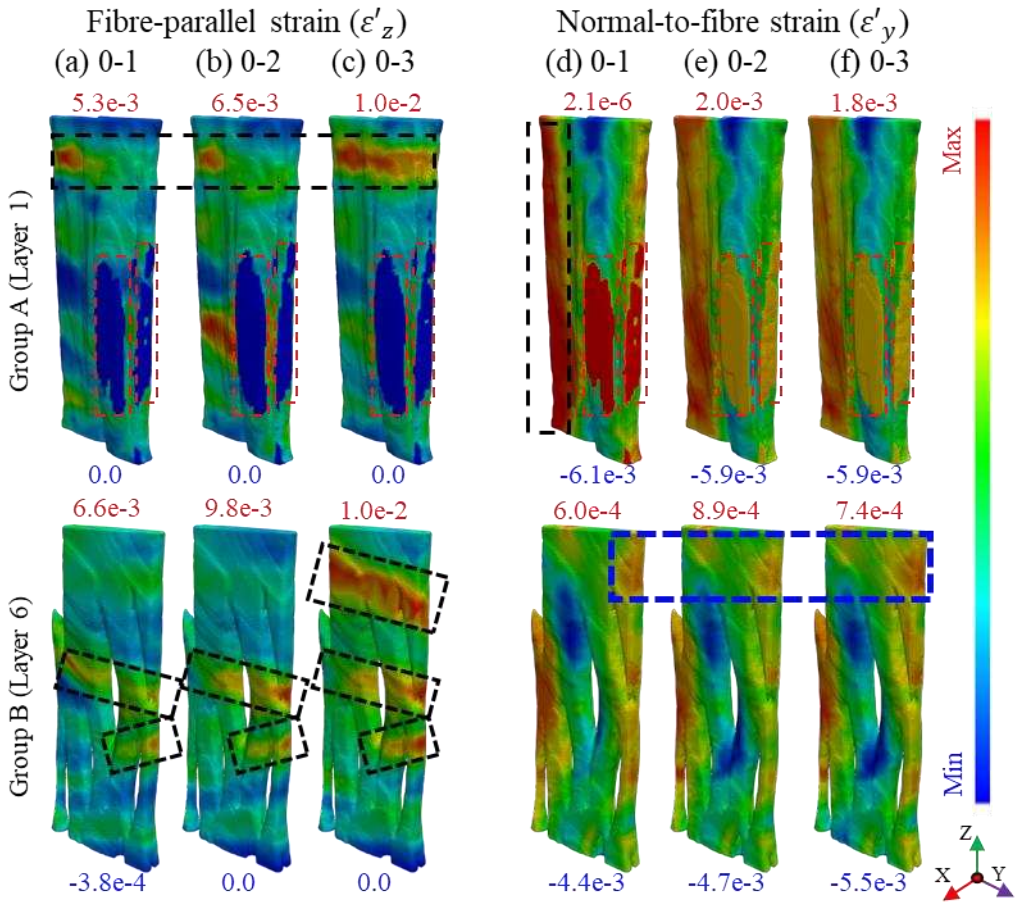

Figure 14: Rotated strain maps in segmented fibre bundles of 0° directional layers 1 (Group A) and 6 (Group B), showing fibre-parallel strain ε'_z (a-c) and fibre-transverse strain ε'_y (d-f), corresponding to correlation steps 0-1, 0-2, 0-3

4 Discussion

4.1 Crack initiation and propagation mechanisms

The in-situ XCT tensile test results revealed that initial cracks in the TFP composite formed at stress level between 37.5% and 50% σ_{UTS} (around 190 MPa). This stress range aligns closely with findings from [23], where stitched composite laminates with varying stitching densities exhibited initiation of 90° cracks between approximately 180 MPa and 220 MPa, whereas ±45° off-axis cracks initiated between roughly 295 MPa and 333 MPa. Initial cracks predominantly initiated near the specimen edges (Figures 5 (a) and 6), consistent with observations reported in [23].

The image segmentation process implemented in this study facilitated precise identification of the initial crack locations, showing their formation within fibre bundles, resin-rich areas, and within stitching threads next to fibre bundles (Figure 5 (a)). Crack paths closely follow local fibre directions and are predominantly located inside the carbon fibre bundles (Figure 5), consistent with observations in other biaxially reinforced composites [24]. In contrast, cracks originating from resin-rich zones or stitching threads at 50% SFR showed limited expansion up to 95% SFR, consistent with prior observations [23]. Conversely, cracks within fibre bundles propagated relatively rapidly, initially through off-axis layers and subsequently through longitudinal layers, with the crack volume fraction exhibiting exponential growth, (Figure 8). This observation supports previous findings that rapid fracture in stitched carbon fibre plain weave laminates

predominantly originates from intra-bundle cracks rather than from resin-rich zones [23, 25].

Interlaminar delamination was mainly observed between layers 5 and 6, and layers 4 and 5 (Figure 5 (d)), becoming apparent from 90% SFR (Figure 5 (c)). By comparison, standard CFRP laminates typically exhibit interlaminar delamination initiation around 60% SFR [26]. The delayed and limited occurrence of delamination observed in the current in-situ test may be attributed to through-thickness reinforcement provided by stitching threads, which introduce compressive stresses at ply interfaces through thread tension applied during manufacturing [23]. The asymmetric distribution of interlaminar delamination through the thickness of the TFP composite is further attributed to the asymmetry caused by the base material and the different thicknesses of the two resin-rich top and bottom layers in Figure 1 (b).

Within resin-rich regions surrounding stitching threads (Figure 6 and 7), matrix cracks initiate owing to reduced fibre content and locally disordered fibre arrangement [27], resulting in decreased load-transfer efficiency and increased local stress concentration [28]. Moreover, these regions are often susceptible to microstructural defects arising during manufacturing processes, such as resin shrinkage [29, 30].

As loading approaches failure, the macroscopic stress-strain curve departs from linearity (Figure 10) and the crack volume increases sharply (Figure 8). Widespread delamination and stitching threads rupture diminish the through-thickness constraint (Figure 5 (d)), allowing rapid crack coalescence and global stiffness degradation [31].

4.2 Strain concentration prior to cracks formation

XCT results revealed that the first observable cracks nucleated in layer 5 (+60° orientation), as shown in Figure 5 (a), rather than in the central off-axis layers 3 and 4 (-60° orientation). This deviation can be attributed to the specimen's geometric mid-plane coinciding with layer 5, where highest strain concentrations were recorded for ε_{xx} (Figure 11), indicating that the combination of off-axis fibre orientation and mid-plane constraint promotes stress accumulation, making it a preferential site for intra-bundle crack initiation.

4.3 Crack initiation and strain correlation

To analyse crack formation in relation to strain localisation, the maximum principal strain (ε_1) was extracted from the full strain tensor as an indicator of tensile-driven damage initiation (Figure 12) [20, 32]. For clearer visualisation, the volumetric strain field results were further processed to extract principal strain distributions on the segmented fibre-bundle region of layer 5, where initial cracks appeared at step 3 (50% SFR, Figure 5 (a)), with results shown in Figure 15.

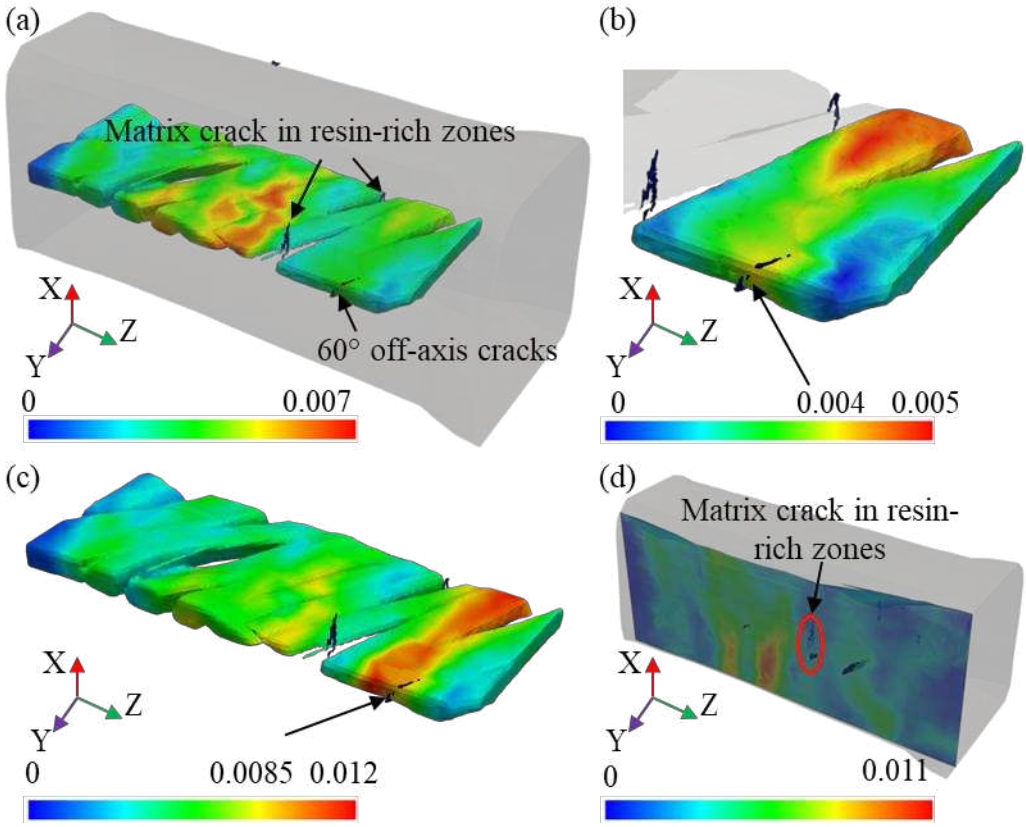

Figure 15: Correlation between maximum principal strain (ε_1) localisation and initial crack formation in the segmented fibre bundles of layer 5: (a) distribution for the correlation step 0-2, 37% SFR, before crack appearance, (b) close-up view of the off-axis crack initiation site in (a), (c) distribution for the correlation step 0-3, 50% SFR, after crack appearance and (d) XZ cross-sectional view of ε_1 in relation to the matrix crack in resin-rich zones

Figure 15 (a) shows the ε_1 distribution obtained at correlation step 0-2 (37% SFR) mapped onto layer 5, overlaid with crack segmentation results from the subsequent loading step (step 3, 50% SFR), with the aim of identifying strain values prior to crack appearance. Results show that the localised principal strain concentration observed in the middle region along the loading direction does not correlate well with the actual crack

initiation location. A detailed view of the crack initiation region (Figure 15 (b)) reveals a principal strain value of approximately 0.004 at the location of the crack prior to its appearance in the subsequent step. Notably, a significant local increase of ε_1 from 0.004 to 0.0085 is observed at the off-axis crack site for the correlation step 0-3 (Figure 15 (c)). In contrast, maximum principal strain distributions exhibited limited correlation with matrix cracks within the resin-rich zones (Figure 15 (d)). This result is attributed primarily to the limited resolution of LG-DVC, particularly in accurately resolving narrow regions, such as the resin-rich zones, which will be further discussed in section 4.5.

Although the maximum first principal strain value (ε_1 = 0.007) identified at correlation step 0-2 (Figure 15(a)) suggested potential crack nucleation in the mid-region along the loading direction, the actual off-axis crack initiated at a location with lower strain intensity (0.004). Furthermore, the location of strain concentration shifted notably from correlation step 0–2 to step 0–3, with the region of maximum strain moving closer to the observed crack initiation site. The reason for that shift might be related to strain compatibility between all layers of the laminate. The analysis of rotated strain components in section 3.2.4 showed that an intense band of strain localisation developed, especially for the fibre-parallel strain component, in the two outermost layers of the laminate (0^o orientation) in the region where a crack appeared in layer 5 (Figure 14). Furthermore, the highest strain values (0.01) were recorded in that localised band of deformation at step 3 when considering the whole laminate. It is therefore possible that the interaction between the various layers led to the formation of a deformation band at a

similar location in layer 5, with localisation of deformation also observed at a similar location in layers 2, 3 and 4 (Figure 13 (d)-(f)).

Although the band of strain concentration matches the region of appearance of the off-axis crack, it remains unclear why the crack specifically appeared at one particular edge of the fibre bundle. For more in-depth analysis, incremental directional strain components ($\varepsilon'_x, \varepsilon'_y, \varepsilon'_z$) for correlation steps 0-1, 1-2, and 2-3 are shown in layer 5 in Figure 16. Results for steps 0-1 and 1-2 show that the maximum strain concentrations for all directional components do not localise at the region where the crack forms (highlighted by the black dashed boxes) at step 3. The next incremental load step does show the significant change in strain concentration location with strain localisation close to the region of crack formation. This also aligns with the results shown in Figures 13 and 14. However, this incremental deformation step shows that the maximum values of the three directional strain components concentrate at the edge of the layer when the crack appeared, especially for the ε'_y component for which the maximum value is located at the very edge of the layer. This particular strain component might therefore be critical for the understanding of crack initiation in TFP composites since it is acting perpendicular to the subsequent crack propagation path along the fibre bundle direction (Figure 5). It is worth pointing out that the total ε'_y strain value of 0.0082 (Figure 13 (f)) recorded at the crack location in Figure 13 is significantly higher than the maximum fibre-transverse strain component values recorded in layers 1 (-0.0015) and 6 (0.00074) in Figure 14, which might explain why cracks did not form in those layers.

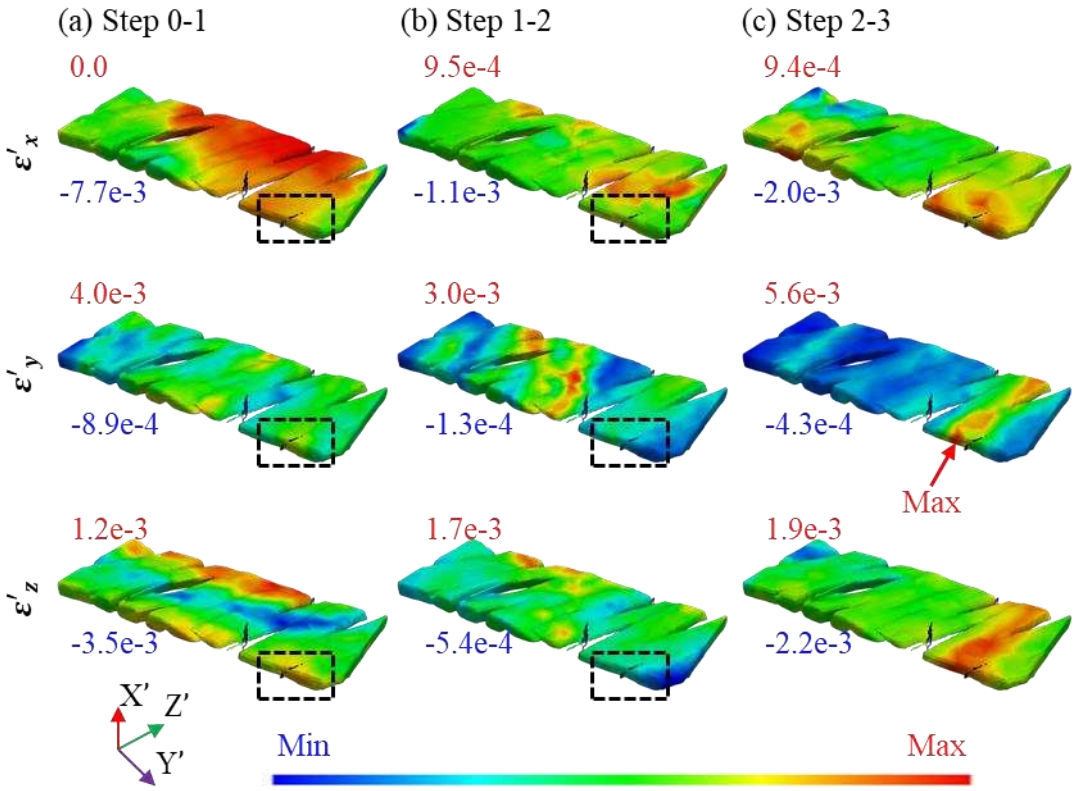

Figure 16: Distributions of through-thickness directional strain (ε'_x), transverse strain (ε'_y), and fibre-parallel strain (ε'_z) on the segmented fibre bundles of layer 5: (a) incremental correlation step 0-1, (b) incremental correlation step 1-2 and (c) incremental correlation step 2-3 (c), with through-thickness directional strain (ε'_x), fibre-transverse strain (ε'_y), and fibre-parallel strain (ε'_z)

4.4 Crack propagation and strain correlation

In contrast to earlier steps, the crack volume increased significantly beyond step 3, making precise correlation between local strain fields and newly formed cracks more challenging. However, crack propagation in layer 5 did follow the band of local deformation shown in Figure 16 (c) at step 0-3 with the crack propagating along the direction of the fibre bundle. Figure 17 shows correlation results between step 0 and step

4, highlighting strain concentrations across the specimen. Although the maximum first principal strain value reached 0.066, the peak value was highly localised and thus did not represent the overall strain distribution effectively (Figure 12 (d)). Most regions exhibiting high strain localisation show values around 0.033, which is considerably greater than the maximum strain observed at step 3 (0.012, Figure 15 (c)). Strain localisation observed in Figure 17 (a) predominantly corresponds to layers 3 and 4. The high-strain regions are primarily located near the sample edges, associated with connected cracks particularly evident in the transition region between the gauge length and the specimen shoulder (red ellipses, Figure 17 (b)). Although a spatial correlation between strain hotspots and off-axis intra-bundle cracks was still identifiable, the increased damage complexity for latter loading stages limited clear one-to-one matching between strain localisation and individual cracks.

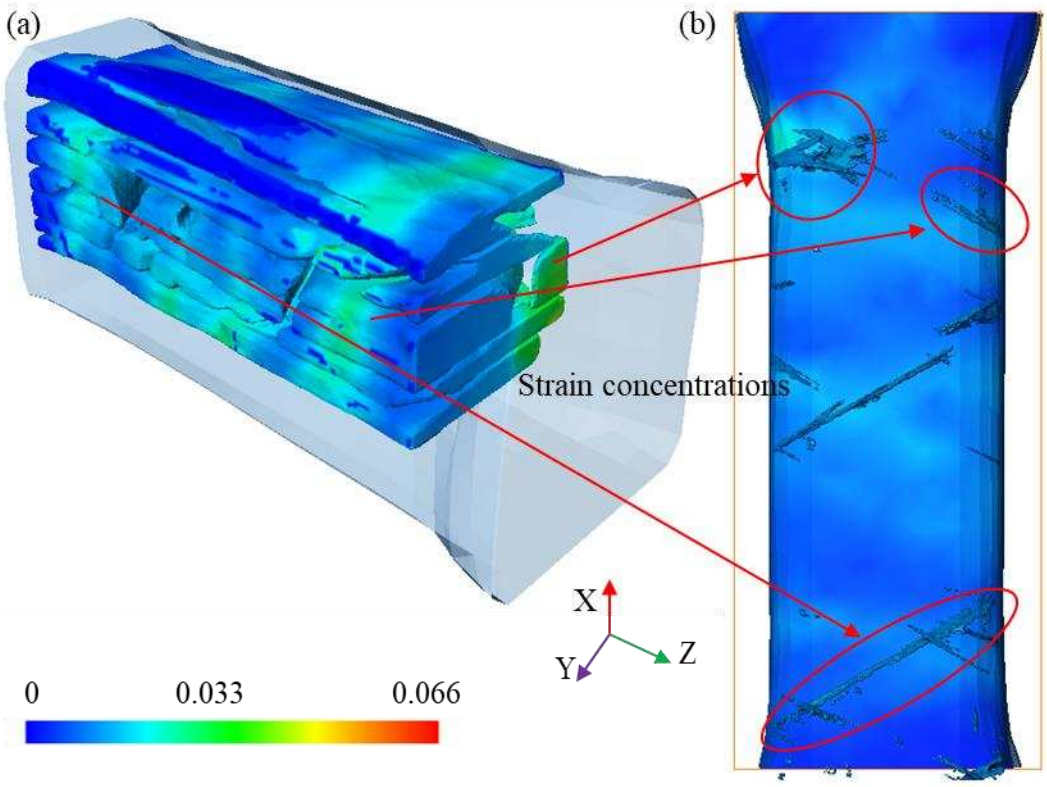

Figure 17: Correlation between cracks and maximum principal strain (ε_1) localisation at 75% SFR. (a) 3D view of the ε_1 strain field distribution. Localised high-strain regions are identified. (b) Top view of the ε_1 field showing the correspondence between cracks and areas of strain concentration (circled in red). The colour scale represents ε_1 values ranging from 0 (blue) to 0.066 (red)

Localised strain concentrations are strongly influenced by structural heterogeneities in the composite, such as resin-rich zones, fibre misalignments, and fibre volume fraction variations [7] induced by the stitching threads. These features are intrinsic to TFP composites and are known to significantly influence the initiation and progression of damage [23]. Additionally, areas exhibiting higher strain concentrations were frequently observed in regions where fibres were predominantly orientated parallel to the direction

of crack propagation (Figure 15 and 17). These findings suggest that DVC-based strain analysis is an effective tool for identifying crack-prone regions within complex composite architectures [9]. In particular, the ability to detect early-stage strain localisation before visible crack formation highlights the potential of this technique for predictive damage assessment. The interplay between strain evolution and internal structure will be further discussed in the context of material design and failure mitigation strategies in the following sections.

4.5 Evaluation of DVC and method suitability

The accuracy and reliability of the applied DVC methodology were systematically assessed through a quantitative uncertainty analysis. Repeated scans under unloaded conditions (step 0–0) were used to evaluate the sensitivity of the local DVC (L-DVC) approach with varying sub-volume sizes. As shown in Figure 9, increasing the sub-volume size generally reduced the standard deviation of both displacement and strain values, indicating improved precision. However, excessively large sub-volumes (>71 voxels) led to increased uncertainty, likely due to over-smoothing effects and diminished sensitivity to local deformation gradients. This observation aligns with prior studies indicating that, in regions of nonuniform deformation, large sub-volumes coupled with low-order shape functions can induce significant systematic errors in displacement measurements [33].

A sub-volume size of 41 voxels was selected as an optimal compromise between accuracy and spatial resolution, providing standard deviations in displacement below 0.2 voxels

and strain errors within the range of 10^{-4} to 10^{-3} με. These values are consistent with the reported performance of DVC in other high-resolution XCT studies [34], confirming the method robustness.

While the DVC approach was effective in mapping internal deformation fields with high accuracy, limitations remain. The spatial resolution is constrained by the voxel size and sub-volume parameters. DVC inherently evaluate similarities between two image volumes in terms of their overall greyscale value distributions. This reliance introduces limitations when analysing resin-rich zones, where the inherent low-density resin exhibits minimal contrast and lacks distinct internal features [35, 36]. Consequently, detecting local strain concentrations within these resin-rich regions becomes challenging (Figure 15 (d)), particularly when cracks propagate through them, as the greyscale intensities of cracks and surrounding resin may become indistinguishable. This reducing contrast can potentially compromise the accuracy and sensitivity of strain measurements obtained via DVC.

4.6 Implications for composite design and structural integrity

The experimental results presented in this study reveal critical insights for the structural design of TFP composites. Crack initiation was shown to correlate strongly with local strain concentration and structural heterogeneity, especially in regions affected by stitching threads. These findings indicate that the inherent complexity of the TFP architecture, while offering geometrical flexibility, may compromise damage tolerance if not carefully managed.

One key observation was that the first cracks appeared in the centrally located layer 5, with a 60° fibre orientation. This suggests that modifying the layup sequence, such as placing a 0° ply at the mid-thickness position of laminates, may reduce the likelihood of early crack formation by distributing axial loads more uniformly and limiting through-thickness strain concentration.

The presence of stitching threads was associated with early matrix cracking in resin-rich zones (Figure 5 (a) and 6). To mitigate such defects, future design strategies could limit the number of stitching locations in structurally critical or edge-near regions. Alternatively, optimising stitch parameters such as spacing, thread tension, or orientation may reduce local void content and improve matrix continuity.

The ability of DVC to resolve internal strain distributions prior to visible damage highlights its potential as a diagnostic tool for TFP composite development. Specifically, DVC-derived strain fields provide essential validation data for multiscale computational models [37] designed to predict fracture initiation, damage progression, and the ultimate strength of TFP composites. Such validated models can significantly inform structural design decisions and support the optimisation of manufacturing parameters. These capabilities position DVC as a valuable asset in advancing the structural reliability of next-generation fibre-reinforced composites.

Overall, the insights gained from this work contribute to a more informed design framework for TFP composites, enabling the balance between manufacturing feasibility

and structural performance to be achieved more effectively for high-demand applications such as in the aerospace and automotive industries.

5 Conclusion

The experimental methodology developed in this work combining in-situ tensile testing inside an XCT microscope with DVC has enabled the first characterisation of damage development in a TFP composite in relation to volumetric full-field strain distribution measurements. A bespoke segmentation of the phases with mapping of 3D strain distributions computed using a LG-DVC algorithm across multiple loading steps has provided new insight into the mechanisms of crack initiation and propagation in complex fibre architectures:

- The early stage of crack formation was captured at an applied stress below 50% of the UTS with damage appearing close to the edge of the specimen in fibre bundles orientated at 60° with respect to the loading direction in the $[0/60/-60]_s$ laminate, in resin-rich regions and within stitching threads.
- Complex strain distributions in the heterogeneous internal structure of the TFP composite were shown to progressively concentrate into an intense band of deformation correlating with the crack location in the fibre bundle. This band of localised strain concentration was observed in all four ±60° plies of the six-ply layup. Both the maximum principal strain value at crack initiation and the value of the local strain component perpendicular to the crack were about 0.008.

- Crack propagation was mainly observed within fibre bundles along the fibre direction, with the initial crack propagating along the band of localised deformation highlighted by DVC. The crack volume rate increases exponentially beyond 50% of the UTS with propagation mainly in the ±60° plies followed by damage of the 0° plies at the end of the test. Very limited delamination was observed towards the end of the test, beyond 90% of the UTS.
- Fibre bundle orientation, the offset between the actual laminate mid-plane and the designed lay-up, and stitching pattern were identified as key factors, influencing damage development. Design modifications such as placing 0° plies at the laminate mid-thickness and reducing the stitching density near the edges of the specimen are promising strategies for enhancing the structural integrity of TFP composites.

In addition, the DVC results provide a valuable foundation for the future development and validation of multiscale, physically-based models aimed at predicting the strength of TFP composites. Such models can be used to guide manufacturing optimisation and enhance the structural performance of TFP composites for lightweight applications.

Acknowledgements

Authors would like to thank The University of Sheffield Tomography Centre (STC) and its funding from EPSRC (EP/T006390/1). For the purpose of open access, the author has applied a Creative Commons Attribution (CCBY) licence to any Author Accepted Manuscript version arising.

References

[1] Mattheij, P., Gliesche, K. and Feltin, D., 1998. Tailored fiber placement-mechanical properties and applications. *Journal of Reinforced Plastics and Composites*, *17*(9), pp.774-786. https://doi.org/10.1177/073168449801700901.

[2] El-Dessouky, H.M., Saleh, M.N., Gautam, M., Han, G., Scaife, R.J. and Potluri, P., 2019. Tailored fibre placement of commingled carbon-thermoplastic fibres for notch-insensitive composites. *Composite structures*, *214*, pp.348-358. https://doi.org/10.1016/j.compstruct.2019.02.043.

[3] Temmen, H., Degenhardt, R. and Raible, T., 2006. Tailored fibre placement optimization tool.

[4] Nomura, T., Spickenheuer, A., Yoshikawa, K., Kawamoto, A. and Iwano, Y., 2020. Design and fabrication of lightweight automotive parts with continuous fiber composite using topology optimization and tailored fiber placement. Transactions of Society of Automotive Engineers of Japan, 51(1). https://doi.org/10.1299/mej.24-00008.

[5] Spickenheuer, A., Scheffler, C., Bittrich, L., Haase, R., Weise, D., Garray, D. and Heinrich, G., 2017. Tailored fiber placement in thermoplastic composites. *Technologies for Lightweight Structures (TLS)*, *1*(2). https://doi.org/10.21935/tls.v1i2.95.

[6] Coppola, A.M., Huelskamp, S.R., Tanner, C., Rapking, D. and Ricchi, R.D., 2023. Application of tailored fiber placement to fabricate automotive composite components with complex geometries. Composite Structures, 313, p.116855. https://doi.org/10.1016/j.compstruct.2023.116855.

[7] Uhlig, K., Tosch, M., Bittrich, L., Leipprand, A., Dey, S., Spickenheuer, A. and Heinrich, G., 2016. Meso-scaled finite element analysis of fiber reinforced plastics made by Tailored Fiber Placement. *Composite Structures*, *143*, pp.53-62. https://doi.org/10.1016/j.compstruct.2016.01.049.

[8] Mohammadi, R., Assaad, M., Imran, A. and Fotouhi, M., 2024. Fractographic analysis of damage mechanisms dominated by delamination in composite laminates: A comprehensive review. *Polymer Testing*, p.108441. https://doi.org/10.1016/j.polymertesting.2024.108441.

[9] Holmes, J., Sommacal, S., Das, R., Stachurski, Z. and Compston, P., 2023. Digital image and volume correlation for deformation and damage characterisation of fibre-reinforced composites: A review. *Composite Structures*, *315*, p.116994. https://doi.org/10.1016/j.compstruct.2023.116994.

[10] Bay, B.K., 2008. Methods and applications of digital volume correlation. *The Journal of Strain Analysis for Engineering Design*, *43*(8), pp.745-760. https://doi.org/10.1243/03093247JSA436.

[11] Lee, S., Jo, E. and Ji, W., 2020. Digital volume correlation technique for characterizing subsurface deformation behavior of a laminated composite. *Composites Part B: Engineering*, *194*, p.108052. https://doi.org/10.1016/j.compositesb.2020.108052.

[12] Holmes, J., Sommacal, S., Stachurski, Z., Das, R. and Compston, P., 2022. Digital image and volume correlation with X-ray micro-computed tomography for deformation

and damage characterisation of woven fibre-reinforced composites. *Composite Structures*, *279*, p.114775. https://doi.org/10.1016/j.compstruct.2021.114775.

[13] ThermoScientific Avizo Software 9 User's Guide, 2018 (https://assets.thermofisher.com/TFS-Assets/MSD/Product-Guides/user-guide-Avizo-software.pdf, accessed on 21.02.2019).

[14] Buljac, A., Jailin, C., Mendoza, A., Neggers, J., Taillandier-Thomas, T., Bouterf, A., Smaniotto, B., Hild, F. and Roux, S., 2018. Digital volume correlation: review of progress and challenges. *Experimental Mechanics*, *58*, pp.661-708. https://doi.org/10.1007/s11340-018-0390-7.

[15] Yang, J., Hazlett, L., Landauer, A.K. and Franck, C., 2020. Augmented lagrangian digital volume correlation (ALDVC). *Experimental Mechanics*, *60*(9), pp.1205-1223. https://doi.org/10.1007/s11340-020-00607-3.

[16] Wang, Y., Chen, Q., Luo, Q., Li, Q. and Sun, G., 2024. Characterizing damage evolution in fiber reinforced composites using in-situ X-ray computed tomography, deep machine learning and digital volume correlation (DVC). *Composites Science and Technology*, *254*, p.110650. https://doi.org/10.1016/j.compscitech.2024.110650.

[17] Wang, Y., Chen, Q., Luo, Q., Li, Q. and Sun, G., 2024. Characterizing damage evolution in fiber reinforced composites using in-situ X-ray computed tomography, deep machine learning and digital volume correlation (DVC). Composites Science and Technology, 254, p.110650. https://doi.org/10.1016/j.compscitech.2024.110650.

[18] Niu, G., Zhu, R., Lei, H., Zhang, R., Wang, P., Qu, Z. and Fang, D., 2022. Internal damage evolution investigation of C/SiC composites using in-situ tensile X-ray computed tomography testing and digital volume correlation at 1000° C. *Composites Part A: Applied Science and Manufacturing*, *163*, p.107247. https://doi.org/10.1016/j.compositesa.2022.107247.

[19] van Dijk, N.P., Wu, D., Persson, C. and Isaksson, P., 2019. A global digital volume correlation algorithm based on higher-order finite elements: Implementation and evaluation. International Journal of Solids and Structures, 168, pp.211-227. https://doi.org/10.1016/j.ijsolstr.2019.03.024.

[20] Wan, Y., Madi, S.E., Madi, K., Soete, J., Takahashi, J., Lomov, S.V. and Swolfs, Y., 2025. Spatial strain distribution and in-situ damage analysis of sheet moulding compounds based on Digital Volume Correlation. *Composites Part B: Engineering*, p.112220. https://doi.org/10.1016/j.compositesb.2025.112220.

[21] Kollar, L.P. and Springer, G.S., 2003. *Mechanics of composite structures*. Cambridge university press. DOI: 10.1017/CBO9780511547140.

[22] Mao, L., Liu, H., Lei, Y., Wu, J., Ju, Y. and Chiang, F.P., 2021. Evaluation of global and local digital volume correlation for measuring 3D deformation in rocks. Rock Mechanics and Rock Engineering, 54(9), pp.4949-4964. 10.1007/s00603-021-02517-9. https://doi.org/10.1007/s00603-021-02517-9.

[23] Yudhanto, A., Lubineau, G., Ventura, I.A., Watanabe, N., Iwahori, Y. and Hoshi, H., 2015. Damage characteristics in 3D stitched composites with various stitch parameters

under in-plane tension. *Composites Part A: Applied Science and Manufacturing*, *71*, pp.17-31. https://doi.org/10.1016/j.compositesa.2014.12.012.

[24] Holmes, J., Sommacal, S., Das, R., Stachurski, Z. and Compston, P., 2022. Characterisation of off-axis tensile behaviour and mesoscale deformation of woven carbon-fibre/PEEK using digital image correlation and X-ray computed tomography. *Composites Part B: Engineering*, *229*, p.109448. https://doi.org/10.1016/j.compositesb.2021.109448.

[25] Yudhanto, A., Watanabe, N., Iwahori, Y. and Hoshi, H., 2012. The effects of stitch orientation on the tensile and open hole tension properties of carbon/epoxy plain weave laminates. *Materials & Design*, *35*, pp.563-571. https://doi.org/10.1016/j.matdes.2011.09.013.

[26] Scott, A.E., Mavrogordato, M., Wright, P., Sinclair, I. and Spearing, S.M., 2011. In situ fibre fracture measurement in carbon–epoxy laminates using high resolution computed tomography. *Composites science and technology*, *71*(12), pp.1471-1477. https://doi.org/10.1016/j.compscitech.2011.06.004.

[27] Sacchetti, F., Grouve, W.J., Warnet, L.L. and Villegas, I.F., 2018. Effect of resin-rich bond line thickness and fibre migration on the toughness of unidirectional Carbon/PEEK joints. *Composites Part A: Applied Science and Manufacturing*, *109*, pp.197-206. https://doi.org/10.1016/j.compositesa.2018.02.035.

[28] Mahmood, A.S., Summerscales, J. and James, M.N., 2022. Resin-rich volumes (RRV) and the performance of fibre-reinforced composites: A review. *Journal of Composites Science*, *6*(2), p.53. https://doi.org/10.3390/jcs6020053.

[29] Dong, C.S. and Tsai, T.C., 2010. Formation of resin-rich zones in composites processing. *Advanced Materials Research*, *123*, pp.543-546. https://doi.org/10.4028/www.scientific.net/AMR.123-125.543.

[30] Tsujimoto, A., Barkmeier, W.W., Takamizawa, T., Latta, M.A. and Miyazaki, M., 2016. Mechanical properties, volumetric shrinkage and depth of cure of short fiber-reinforced resin composite. *Dental materials journal*, *35*(3), pp.418-424. https://doi.org/10.4012/dmj.2015-280.

[31] Tan, K.T., Yoshimura, A., Watanabe, N., Iwahori, Y. and Ishikawa, T., 2013. Effect of stitch density and stitch thread thickness on damage progression and failure characteristics of stitched composites under out-of-plane loading. *Composites science and technology*, *74*, pp.194-204. https://doi.org/10.1016/j.compscitech.2012.11.001.

[32] Chen, Y., Shi, Y., Chateau, C. and Marrow, J., 2021. In situ X-ray tomography characterisation of 3D deformation of C/C-SiC composites loaded under tension. *Composites Part A: Applied Science and Manufacturing*, *145*, p.106390. https://doi.org/10.1016/j.compositesa.2021.106390.

[33] Pan, B. and Wang, B., 2020. Some recent advances in digital volume correlation. *Optics and Lasers in Engineering*, *135*, p.106189. https://doi.org/10.1016/j.optlaseng.2020.106189.

[34] Forna-Kreutzer, J.P., Ell, J., Barnard, H., Pirzada, T.J., Ritchie, R.O. and Liu, D., 2021. Full-field characterisation of oxide-oxide ceramic-matrix composites using X-ray computed micro-tomography and digital volume correlation under load at high temperatures. *Materials & Design*, *208*, p.109899. https://doi.org/10.1016/j.matdes.2021.109899.

[35] Zwanenburg, E.A., Norman, D.G., Qian, C., Kendall, K.N., Williams, M.A. and Warnett, J.M., 2023. Effective X-ray micro computed tomography imaging of carbon fibre composites. *Composites Part B: Engineering*, *258*, p.110707. https://doi.org/10.1016/j.compositesb.2023.110707.

[36] Lee, S., Jo, E. and Ji, W., 2020. Digital volume correlation technique for characterizing subsurface deformation behavior of a laminated composite. *Composites Part B: Engineering*, *194*, p.108052. https://doi.org/10.1016/j.compositesb.2020.108052.

[37] Dall'Ara, E. and Tozzi, G., 2022. Digital volume correlation for the characterization of musculoskeletal tissues: Current challenges and future developments. *Frontiers in Bioengineering and Biotechnology*, *10*, p.1010056. https://doi.org/10.3389/fbioe.2022.1010056.